SOC-Based Simulation of 3D MIMO Mobile-to-Mobile Fading Channels: A Riemann Sum Approach

CARLOS A. GUTIÉRREZ [1] **(Senior Member, IEEE),**
RAÚL A. FABÍAN-RODRÍGUEZ [1] **, FRANCISCO R. CASTILLO-SORIA** [1] **,**
CESAR A. AZURDIA-MEZA [2] **(Member, IEEE), AND PABLO ADASME** [3]

[1]Faculty of Science, Universidad Autónoma de San Luis Potosí, San Luis Potosi 78295, Mexico
[2]Department of Electrical Engineering, Universidad de Chile, Santiago 8370451, Chile
[3]Department of Electrical Engineering, Universidad de Santiago de Chile, Santiago 9170124, Chile

CORRESPONDING AUTHOR: CARLOS A. GUTIÉRREZ (e-mail: cagutierrez@ieee.org).

ABSTRACT The Riemann sum method (RSM) was introduced almost two decades ago as an efficient parameter computation method for the design of narrowband multiple-input multiple-output (MIMO) mobile fading channel simulators based on the sum-of-cisoids (SOC) principle. This method has been shown to be more accurate and less computationally expensive than other methods based on the SOC principle. However, the RSM was formulated by assuming uniform linear antenna arrays and a two-dimensional geometrical propagation environment. These assumptions impose important limitations, as the mobile communication systems are evolving to provide service in a variety of three-dimensional (3D) environments by employing different antenna array configurations. This article presents two generalized versions of the RSM that remove such limitations. One version follows the deterministic approach of the original RSM, which is specific to the design of ergodic SOC-based simulators for wide-sense stationary (WSS) channels. The other version is inspired by a stochastic approach that enables the non-ergodic simulation of WSS channels and which can be extrapolated to the simulation of non-WSS channels. Simulation results presented here demonstrate that both generalizations provide an excellent approximation to the envelope distribution and correlation properties of 3D narrowband MIMO mobile-to-mobile fading channels, regardless of the antenna array configuration and the propagation environment's geometry.

INDEX TERMS Channel simulators, fading channels, multiple-input multiple-output channels, mobile radio communications, mobile-to-mobile communications, sum-of-sinusoids process, wide-sense stationary channels, vehicular communications.

I. INTRODUCTION

The design of mobile fading channel simulators is a constantly evolving research topic, whose applications are instrumental for the computer-aided analysis of modern mobile communication systems. One of the most important approaches to the design of such simulators is based on the sum-of-sinusoids (SOS) principle, which was originally introduced by Rice in [1], [2] for the modeling of colored Gaussian noise. The wide acceptance of channel simulators based on a SOS model, or on a sum of complex sinusoids (cisoids) model [3], is

due in part to the ease with which these simulators can be implemented in both software and hardware [4], [5], [6]. In addition, the mathematical description of a sum of cisoids (SOC) is identical to that of the superposition of electromagnetic time-harmonic waves, which gives these models a clear physical meaning [7].

The SOC-based channel simulators can be classified in three different groups: *i*) non-stationary, *ii*) ergodic *iii*) and non-ergodic stationary simulators. The emergence of mobile wideband communication systems that rely on highly

dynamic links, such as short-range communication systems for connected vehicles [8], has recently placed the spotlight on the design of non-stationary channel simulators [9], [10], [11]. However, the development of new simulation models for stationary channels continues to be relevant, as under some conditions, the mobile fading channel presents the characteristics of a wide-sense stationary (WSS) random process. In particular, it is shown in [12] and [13] that the WSS condition can be invoked for the modeling and simulation of frequency-nonselective channels whenever the assumptions of uniform motion and plane-wave propagation apply. A WSS channel simulator is therefore pertinent, e.g., for the analysis of modern medium- and long-range narrowband communication systems, such as those in [14], [15]. Moreover, non-stationary channel simulators are oftentimes built upon reconfigurable WSS simulators by following a multi-state Markov chain approach, where the response of the non-stationary channel is characterized by a WSS random process for each state of the chain, e.g., see [16].

The difference between ergodic and non-ergodic stationary simulators is that the former generate channel waveforms (sample functions) whose time averages provide a close approximation to the ensemble averages of the reference channel model in every simulation run. Non-ergodic stationary simulators do not possess this feature, and it is therefore necessary to compute the average of multiple realizations to obtain a good approximation to the reference model's ensemble averages [17]. Nevertheless, the accuracy of the ergodic SOC-based channel simulators depends on how long in time are the generated channel waveforms; the longer the generated waveforms, the more accurate the simulator is in approximating the channel's ensemble averages [18]. This characteristic can suppose an impractical condition for the analysis of communication systems if the channel's stationarity interval in time is short, as is the case of vehicular communication systems. A non-ergodic stationary SOC model offers a better solution for the simulation of mobile fading channels having a short time-stationarity interval.

Several different parameter computation methods (PCMs) have been developed for the SOC-based simulation of WSS mobile fading channels [7], [19]. Among them, the Riemann sum method (RSM) [20] stands out for its simplicity and accuracy in emulating the channel's correlation properties under both isotropic and anisotropic scattering conditions. The RSM was introduced almost two decades ago as an efficient PCM for ergodic SOC-based simulators of narrowband multiple-input multiple-output (MIMO) mobile fading channels [21]. In contrast to other methods, such as the equal areas method [22] or the L_p-norm (LPNM) method [23], the RSM allows the calculation of the simulation model's parameters (amplitudes and Doppler frequencies) without relying on numerical optimization methods. This makes the RSM more efficient and easier to reconfigure, as demonstrated in [20]. However, the RSM was formulated by assuming uniform linear antenna arrays and a two-dimensional geometrical propagation environment with scatterers arranged according

to the one-ring scattering model. These assumptions impose important limitations, as the mobile communication systems are evolving to provide connectivity in three dimensions (3D), such as that required to connect terminals at ground level with drones or with terrestrial antennas mounted on elevated structures, and employing different antenna array configurations [24].

This paper eliminates such limitations by introducing two generalized versions of the RSM with respect to (w.r.t.) the simulation of narrowband MIMO mobile-to-mobile (M2M) fading channels under 3D propagation conditions. One version, called the deterministic RSM (DRSM), follows the same deterministic approach of the original RSM, which is specific to the design of ergodic SOC-based simulators for WSS channels.[1] The other version, called the randomized RSM (RRSM), is inspired by a stochastic approach that enables the non-ergodic simulation of WSS channels. This latter version can easily be extrapolated to the simulation of non-WSS channels by applying the concepts discussed in [16], although only the stationary case is addressed in detail in this paper to facilitate the understanding of the idea behind the RRSM. The excellent performance of these two new PCMs is demonstrated w.r.t. the emulation of the envelope distribution, the time autocorrelation function (TACF), and the space cross-correlation function (SCCF) of a 3D narrowband MIMO M2M fading channel model by considering different configurations for both the antenna arrays and the geometry of the propagation environment. Owing to their flexibility and good performance, the DRSM and the RRSM can easily be applied to the performance analysis of emerging narrowband transmission systems, such as those presented in [14], [15], [26], [27], [28].[2]

The remainder of the paper is organized as follows: Section II presents an overview of the mathematical channel model that has been adopted as a reference for the generalization of the RSM. The DRSM and the RRSM are presented in Sections III and IV, respectively. The performance of both PCMs is numerically evaluated in Section V w.r.t. their accuracy in emulating the envelope distribution and the correlation properties of the reference channel model. The main conclusions of this work are given in Section VI.

Notation: Scalar variables are written in plain face, bold lowercase letters and symbols are reserved for vectors, and matrices are denoted by bold uppercase fonts. Vectors are defined in spherical coordinates as ordered triplets of the form (r, θ, ϕ), where $r \in [0, \infty)$, $\theta \in [0, \pi)$, and $\phi \in [0, 2\pi)$ are the vector's magnitude, inclination angle, and azimuth angle, respectively. Unit vectors are written with a circumflex. The canonical vectors of the rectangular system of coordinates are given by $\hat{\mathbf{x}} = (1, \pi/2, 0)$, $\hat{\mathbf{y}} = (1, \pi/2, \pi/2)$ and $\hat{\mathbf{z}} =$

---

[1] A preliminary version of the DRSM that was formulated under the assumptions of ULAs and the geometric sphere scattering model was presented previously in [25].

[2] A narrowband transmission system is understood in this paper as a system whose channel response can be considered nearly flat (frequency-nonselective) for the purposes of signal demodulation and detection.

(1, 0, 0). The component of a vector $\mathbf{v}$ in a given dimension, r, is denoted by $\langle \mathbf{v} \rangle_r$. The operators $\| \cdot \|$, $\| \cdot \|_F$, $\circledast$, $(\cdot)^*$, $(\cdot)^\top$, vec$\{\cdot\}$, $|\cdot|$, $\mathcal{E}\{\cdot\}$, sup$\{\cdot\}$, and $\otimes$ stand for the Euclidean norm, the Frobenius norm, the vector scalar product, the complex conjugate, the matrix transpose, the column vector resulting from the vertical stacking of a matrix's columns, the scalar absolute value, the statistical expectation, the supremum, and the Cartesian product, respectively. In addition, $\lceil \cdot \rceil$ and $\lfloor \cdot \rfloor$ indicate, in that order, the nearest integer toward $+\infty$ and the nearest integer toward $-\infty$. The set of real, complex, and non-negative integer numbers are denoted by $\mathbb{R}$, $\mathbb{C}$, and $\mathbb{Z}_+$, respectively.

II. THE REFERENCE 3D MIMO M2M CHANNEL MODEL

A. MATHEMATICAL MODEL OF THE CHANNEL TRANSFER FUNCTION

Our reference point for the reformulation of the RSM is the generic MIMO M2M Rayleigh fading channel model proposed in [13]. We consider a narrowband MIMO communications system comprising $N \in \mathbb{Z}_+$ transmitting antennas and $M \in \mathbb{Z}_+$ receiving antennas. The transmitter (T_X) and the receiver (R_X) are assumed to move at a constant velocity $\mathbf{v}_T = \left(v_T, \gamma_T^\theta, \gamma_T^\phi \right)$ and $\mathbf{v}_R = \left(v_R, \gamma_R^\theta, \gamma_R^\phi \right)$, respectively. In turn, the signal transmitted by the nth transmitting antenna is assumed to reach the mth receiving antenna via K non-line-of-sight (NLOS) propagation paths, for $K \in \mathbb{Z}_+$, $n \in \{1, 2, \dots, N\}$, and $m \in \{1, 2, \dots, M\}$. Each NLOS path involves the interaction of the transmitted signal with one interfering object (IO).

The reference geometry for the modeling of the kth propagation path is shown in Fig. 1 [13]. In this figure, the points tagged as $\mathcal{O}$, $\mathcal{O}_T$, and $\mathcal{O}_R$ indicate the location of the origin of our reference right-handed system of coordinates, the initial location of the transmitting antenna array's center of mass, and the initial location of the receiving antenna array's center of mass, respectively. The vectors $\mathbf{d}_T$, $\mathbf{d}_R$, and $\mathbf{d}_k$ describe, in that order, the initial position of the T_X, the R_X and the kth IO. The vectors $\mathbf{p}_0^{(k)} = \left(p_0^{(k)}, \theta_T^{(k)}, \phi_T^{(k)} \right)$ and $\mathbf{q}_0^{(k)} = \left(q_0^{(k)}, \theta_R^{(k)}, \phi_R^{(k)} \right)$ characterize the position of the kth IO as seen from $\mathcal{O}_T$ and $\mathcal{O}_R$, respectively, for $k \in \{1, 2, \dots, K\}$. The initial position of the nth element of the transmitting antenna array, as seen from $\mathcal{O}_T$, is denoted by the vector $\mathbf{a}_T^{(n)} = \left(A_T^{(n)}, \alpha_T^{(n)}, \beta_T^{(n)} \right)$. Likewise, $\mathbf{a}_R^{(m)} = \left(A_R^{(m)}, \alpha_R^{(m)}, \beta_R^{(m)} \right)$ indicates the initial position of the mth element of the receiving antenna array as seen from $\mathcal{O}_R$. Note that this generic description of the array elements' position allows modeling arrays of arbitrary shapes. Appendix A provides details on the particular form of $\mathbf{a}_T^{(n)}$ and $\mathbf{a}_R^{(m)}$ for three relevant array configurations, namely: the uniform linear array (ULA), the uniform circular array (UCA), and the uniform rectangular array (URA).

Under the aforementioned conditions, the transfer function of the frequency-nonselective channel between the nth transmit antenna and the mth receive antenna can be modeled in
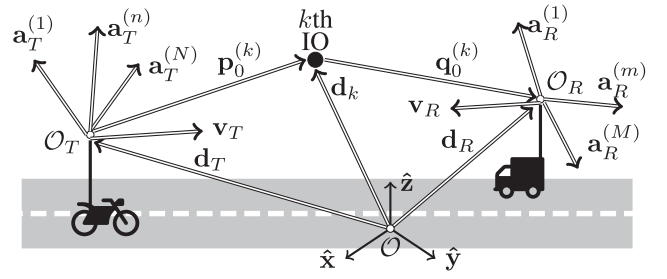

FIGURE 1. Geometry for the modeling of the kth propagation path.

the complex baseband equivalent at the time instant t as

$$H_{m,n}(t) = \sum_{k=1}^{K} g_k e^{-j\left[2\pi f_c \tau_{m,n}^{(k)}(t) + \psi_k \right]}. \tag{1}$$

In this equation, $f_c > 0$ denotes the central frequency of the transmitted passband signal, whereas g_k and ψ_k stand for the attenuation factor and phase shift due to the interaction of the transmitted signal with the kth IO. The attenuation factors, g_k, are modeled by mutually statistically independent and identically distributed (i.i.d.) non-negative random variables. Specifically, we assume that g_k follows a Rayleigh distribution with scale (dispersion) parameter equal to $s_g / \sqrt{2K}$, for $s_g \in (0, \infty)$ [29]. For simplicity, and without loss of generality, we will henceforth assume that $s_g = 1$. Likewise, the phase shifts, ψ_k, are modeled by i.i.d. circular uniform random variables [30]. In turn, $\tau_{m,n}^{(k)}(t)$ stands for the time-varying propagation delay of the signal that propagates from the nth transmit antenna to the mth receive antenna over the kth NLOS propagation path. By assuming the propagation of plane waves, and following [13], we model the propagation delays by

$$\tau_{m,n}^k(t) = \tau_0^{(k)} - \frac{1}{f_c} \left[\Lambda_{m,n}^{(k)} - t \upsilon_D^{(k)} \right] \tag{2}$$

for $k \in \{1, 2, \dots, K\}$, $n \in \{1, 2, \dots, N\}$ and $m \in \{1, 2, \dots, M\}$. The time-invariant variable $\tau_0^{(k)}$ stands for the initial propagation delay of an hypothetical plane wave traveling from $\mathcal{O}_T$ to the kth IO, and from this object to $\mathcal{O}_R$. This propagation delay is given as

$$\tau_0^{(k)} = \frac{\left\| \mathbf{p}_0^{(k)} \right\| + \left\| \mathbf{q}_0^{(k)} \right\|}{\lambda} \tag{3}$$

where λ denotes the carrier signal's wavelength. The variables $\Lambda_{m,n}^{(k)}$ and $\upsilon_D^{(k)}$ are given as:

$$\Lambda_{m,n}^{(k)} = \frac{1}{\lambda} \left[\mathbf{a}_R^{(m)} \circledast \hat{\mathbf{q}}_0^{(k)} - \mathbf{a}_T^{(n)} \circledast \hat{\mathbf{p}}_0^{(k)} \right] \tag{4}$$

$$\upsilon_D^{(k)} = \frac{1}{\lambda} \left[\mathbf{v}_R \circledast \hat{\mathbf{q}}_0^{(k)} - \mathbf{v}_T \circledast \hat{\mathbf{p}}_0^{(k)} \right]. \tag{5}$$

The unit vectors $\hat{\mathbf{p}}_0^{(k)} = \mathbf{p}_0^{(k)} / p_0^{(k)}$ and $\hat{\mathbf{q}}_0^{(k)} = \mathbf{q}_0^{(k)} / q_0^{(k)}$ describe the direction of departure (DOD) and the direction of arrival (DOA) of the plane wave arriving at the R_X over the kth propagation path. The variable $\Lambda_{m,n}^{(k)}$ characterizes the

phase shift due to the spatial displacement of the nth transmit antenna and the mth receive antenna w.r.t. $\mathcal{O}_T$ and $\mathcal{O}_R$, respectively. In turn, $\upsilon_D^{(k)}$ characterizes the frequency shift caused by the Doppler effect due to the motion of the T_X and the R_X.

B. STATISTICAL PROPERTIES OF THE REFERENCE CHANNEL MODEL

The reference 3D channel model defined by (1)–(5) can be adapted to a wide variety of geometrical configurations of the propagation environment depending on the form given to the initial position vectors $\mathbf{p}_0^{(k)}$ and $\mathbf{q}_0^{(k)}$. Appendix B presents a summary of the particular form that these two vectors adopt for two widely accepted geometrical configurations, namely the sphere [31] and the cylinder [32] scattering models. Regardless of the underlying geometry of the propagation environment, we model the vectors $\mathbf{p}_0^{(k)}$ and $\mathbf{q}_0^{(k)}$ as random vectors characterized by joint-probability density functions (PDFs) $f_{P,\Theta,\Phi}^T(p_T, \theta_T, \phi_T)$ and $f_{Q,\Theta,\Phi}^R(q_R, \theta_R, \phi_R)$, respectively. We assume that such position vectors are inter-path independent, meaning that the pair of vectors in $\left\{\mathbf{p}_0^{(k)}, \mathbf{q}_0^{(k)}\right\}$ is mutually statistically independent from the pair of vectors in $\left\{\mathbf{p}_0^{(l)}, \mathbf{q}_0^{(l)}\right\}$, for $k \neq l$. In contrast, $\mathbf{p}_0^{(k)}$ and $\mathbf{q}_0^{(k)}$ are intra-path dependent, i.e., they are mutually statistically dependent, which is a consequence of the geometrical relationship between both vectors; we note that $\mathbf{p}_0^{(k)} = \mathbf{d}_{TR} + \mathbf{q}_0^{(k)}$, where $\mathbf{d}_{TR} = \mathbf{d}_R - \mathbf{d}_T$, $k \in \{1, 2, \ldots, K\}$ (see Fig. 1). We assume that the vectors $\mathbf{d}_T$ and $\mathbf{d}_R$ are deterministic, meaning that the initial positions of the T_X and R_X are known. In addition, we define the magnitude of $\mathbf{q}_0^{(k)}$, $q_0^{(k)} \in \mathbb{R}$, as a real-valued function of the DOA's statistics, as follows

$$q_0^{(k)} = \mathcal{G}\left(\theta_R^{(k)}, \phi_R^{(k)}\right), \quad k \in \{1, 2, \ldots, K\} \tag{6}$$

where the mapping $\mathcal{G} : \mathbb{R}^2 \mapsto \mathbb{R}$ is determined by the geometrical configuration of the propagation environment, as exemplified by (93) and (94) in Appendix B.

The channel transfer function (CTF), $H_{m,n}(t) \in \mathbb{C}$, can then be modeled by a complex-valued Gaussian random process having a mean value, an instantaneous power, a first-order (FO) envelope PDF, and a FO phase PDF equal to:

$$\mu_H(t) \triangleq \mathcal{E}\{H_{m,n}(t)\} = 0, \tag{7}$$

$$\rho_H(t) \triangleq \mathcal{E}\left\{\left|H_{m,n}(t)\right|^2\right\} = \sum_{k=1}^{K} \mathcal{E}\left\{g_k^2\right\} = 1 \tag{8}$$

$$f_Z(z; t) = \frac{2z}{s_g^2} e^{-z^2/s_g^2}, \quad z \in (0, \infty) \tag{9}$$

$$f_\Psi(\psi; t) = \frac{1}{2\pi}, \quad \psi \in [0, 2\pi). \tag{10}$$

In addition, the space-time cross-correlation function (ST-CCF) between $H_{m,n}(t)$ and $H_{l,i}(t)$ is equal to

$$R_{l,m,i,n}(\Delta t) \triangleq \mathcal{E}\left\{H_{m,n}^*(t - \Delta t)H_{l,i}(t)\right\}$$

$$= \int_{\theta_R} \int_{\phi_R} e^{j2\pi \Delta t \upsilon_D(\theta_R, \phi_R)}$$

$$\times e^{j2\pi[\Lambda_{l,i}(\theta_R, \phi_R) - \Lambda_{m,n}(\theta_R, \phi_R)]}$$

$$\times f_{\text{DOA}}^R(\theta_R, \phi_R) \, d\theta_R \, d\phi_R \tag{11}$$

where $f_{\text{DOA}}^R(\theta_R, \phi_R)$ is the PDF characterizing the DOA statistics of the K received plane waves. The Doppler frequency, $\upsilon_D(\theta_R, \phi_R)$, and the spatial displacement terms, $\Lambda_{m,n}(\theta_R, \phi_R)$, are equal to

$$\upsilon_D(\theta_R, \phi_R) = \left[V_R^{(1)} \cos \phi_R + V_R^{(2)} \sin \phi_R\right] \sin \theta_R$$

$$- \left[V_T^{(1)} \cos \phi_T + V_T^{(2)} \sin \phi_T\right] \sin \theta_T$$

$$+ V_R^{(3)} \cos \theta_R - V_T^{(3)} \cos \theta_T \tag{12}$$

$$\Lambda_{m,n}(\theta_R, \phi_R) = \left[W_m^{(1)} \cos \phi_R + W_{l,m}^{(2)} \sin \phi_R\right] \sin \theta_R$$

$$- \left[U_n^{(1)} \cos \phi_T + U_n^{(2)} \sin \phi_T\right] \sin \theta_T$$

$$+ W_m^{(3)} \cos \theta_R - U_n^{(3)} \cos \theta_T \tag{13}$$

for $m \in \{1, 2, \ldots, M\}$ and $n \in \{1, 2, \ldots, N\}$, where:

$$W_m^{(r)} = \frac{1}{\lambda}\langle \mathbf{a}_R^{(m)}\rangle_r, \quad U_n^{(r)} = \frac{1}{\lambda}\langle \mathbf{a}_T^{(n)}\rangle_r \tag{14}$$

$$V_R^{(r)} = \frac{1}{\lambda}\langle \mathbf{v}_R\rangle_r, \quad V_T^{(r)} = \frac{1}{\lambda}\langle \mathbf{v}_T\rangle_r \tag{15}$$

for $r \in \{x, y, z\}$. The inclination angle-of-departure (IAOD), θ_T, and the azimuth angle-of-departure (AAOD), ϕ_T, are also modeled as functions of the DOA, as shown in (16) at the bottom of the page, and (17).

$$\phi_T = \arctan\left(\frac{\langle \mathbf{d}_{TR}\rangle_y + \mathcal{G}(\theta_R, \phi_R)\sin\theta_R\sin\phi_R}{\langle \mathbf{d}_{TR}\rangle_x + \mathcal{G}(\theta_R, \phi_R)\sin\theta_R\cos\phi_R}\right). \tag{17}$$

Two important aspects of our reference channel model are worth highlighting. First, we note that most of the space-time cross-correlation models for narrowband WSS MIMO channels that are available in the open literature are particular solutions of (11)–(17), see, e.g., [33]. It should be noted,

$$\theta_T = \arctan\left(\frac{\sqrt{\left[\langle\mathbf{d}_{TR}\rangle_x + \mathcal{G}(\theta_R, \phi_R)\sin\theta_R\cos\phi_R\right]^2 + \left[\langle\mathbf{d}_{TR}\rangle_y + \mathcal{G}(\theta_R, \phi_R)\sin\theta_R\sin\phi_R\right]^2}}{\langle\mathbf{d}_{TR}\rangle_z + \mathcal{G}(\theta_R, \phi_R)\cos\theta_R}\right) \tag{16}$$

nonetheless, that such correlation models have been obtained under the long-range communications condition, which implies that $\|\mathbf{d}_{TR}\| \gg q_0^{(k)}, \forall k \in \{1, 2, \ldots, K\}$. By invoking this condition, θ_T and ϕ_T can be approximated by:

$$\theta_T \approx \begin{cases} \frac{\pi}{2} - \frac{\mathcal{G}(\theta_R, \phi_R)}{\|\mathbf{d}_{TR}\|} \cos\theta_R, & \theta_R \in [0, \pi/2) \\ \frac{\pi}{2} + \frac{\mathcal{G}(\theta_R, \phi_R)}{\|\mathbf{d}_{TR}\|} \cos\theta_R, & \theta_R \in [\pi/2, \pi) \end{cases} \quad (18)$$

$$\phi_T \approx \frac{\mathcal{G}(\theta_R, \phi_R)}{\|\mathbf{d}_{TR}\|} \sin\theta_R \sin\phi_R. \quad (19)$$

Throughout this paper, and for the sake of generality, we will work with the exact form of the IAOD and AAOD shown in (16) and (17).

Another remarkable aspect of the reference channel model described in this section is that it lends itself for the Monte Carlo simulation of MIMO M2M channels. This task can be accomplished by a direct evaluation of (1)–(6), (16) and (17) provided that a random number generator is available to produce K realizations of the random vector $(1, \theta_R, \phi_R)$ characterizing the DOA (or of the vector $(1, \theta_T, \phi_T)$ that describes the DOD). The implementation of such a random number generator is straightforward if some simplifying assumptions are invoked, such as that involving the statistical independence between the inclination angle of arrival (IAOA), θ_R, and the azimuth angle of arrival (AAOA), ϕ_R [25], [32]. However, for some relevant spherical models, e.g., the von Mises-Fisher (VMF) distribution [30], the implementation of a routine for generating joint outcomes of θ_R and ϕ_R is far from trivial. The intricacies in the implementation of such random number generators affect the reconfigurability of the simulator and represents a major problem when the DOA statistics need to be changed on-the-fly during a simulation run, as required for the simulation of non-WSS channels having a blockwise-stationary structure [16]. Furthermore, the simulation of $H_{m,n}(t; f)$ following a direct Monte Carlo approach is oftentimes an inefficient choice, as this method may present a slow convergence rate of the statistics of the generated MIMO channel waveforms to those of the ensemble [7]. The DRSM and the RRSM are introduced in the following sections as alternatives that enable a more flexible and efficient simulation of 3D MIMO M2M fading channels.

III. THE DRSM FOR THE SOC-BASED SIMULATION OF 3D NARROWBAND MIMO M2M CHANNELS

A. THE ERGODIC SOC-BASED SIMULATION MODEL

The generalization of the original RSM w.r.t. the simulation of the generic 3D narrowband MIMO M2M channel model presented in the previous section is built upon a SOC-based simulation model of the form

$$\widetilde{H}_{m,n}(t) = \sum_{k=1}^{K} \tilde{g}_k e^{-j\tilde{\psi}_k} e^{j2\pi\left[\tilde{\Lambda}_{m,n}^{(k)} - \tilde{v}_D^{(k)} t\right]} \quad (20)$$

where the phases $\tilde{\psi}_k$ are modeled by i.i.d. circular uniform random variables, whereas $\tilde{g}_k$, $\tilde{\Lambda}_{m,n}^{(k)}$ and $\tilde{v}_D^{(k)}$ are deterministic quantities, for $m \in \{1, 2, \ldots, M\}$, $n \in \{1, 2, \ldots, N\}$ and $k \in \{1, 2, \ldots, K\}$. The stochastic process defined by (20) can be identified as a Class II SOC-based simulation model [17] whose mean value, instantaneous power, FO envelope PDF, and FO phase PDF are equal to

$$\mu_{\widetilde{H}}(t) \triangleq \mathcal{E}\left\{\widetilde{H}_{m,n}(t)\right\} = 0 \quad (21)$$

$$\rho_{\widetilde{H}}(t) \triangleq \mathcal{E}\left\{|\widetilde{H}_{m,n}(t)|^2\right\} = \sum_{k=1}^{K} \tilde{g}_k^2 \quad (22)$$

$$f_{\widetilde{Z}}(z; t) = z(2\pi)^2 \int_0^\infty \left[\prod_{k=1}^{K} J_0(2\pi|\tilde{g}_k|x)\right] \\ \times J_0(2\pi zx)x \, \mathrm{d}x, \quad z \geq 0 \quad (23)$$

$$f_{\widetilde{\Psi}}(\psi; t) = \frac{1}{2\pi}, \quad \psi \in [0, 2\pi) \quad (24)$$

where $J_0(\cdot)$ is the Bessel function of the first kind and zeroth order [17]. In turn, the ST-CCF between $\widetilde{H}_{m,n}(t)$ and $\widetilde{H}_{l,i}(t)$ is equal to

$$\widetilde{R}_{l,m,i,n}(\Delta t) \triangleq \mathcal{E}\left\{\widetilde{H}_{m,n}^*(t - \Delta t)\widetilde{H}_{l,i}(t)\right\}$$

$$= \sum_{k=1}^{K} \tilde{g}_k^2 e^{j2\pi\left[\tilde{\Lambda}_{l,i}^{(k)} - \tilde{\Lambda}_{m,n}^{(k)} + \Delta t\tilde{v}_D^{(k)}\right]}. \quad (25)$$

The Class II of SOC models is comprised of mean-ergodic and auto-correlation ergodic stochastic process [17]. It can be easily verified that the $M \cdot N$ random processes in $\{\widetilde{H}_{m,n}(t)\}$ are also cross-correlation ergodic, meaning that

$$\widetilde{R}_{l,m,i,n}(\Delta t) = \overline{R}_{l,m,i,n}^{(\ell)}(\Delta t), \quad \forall \ell \in \mathbb{Z}_+ \quad (26)$$

where

$$\overline{R}_{l,m,i,n}^{(\ell)}(\Delta t) \triangleq \lim_{T \to \infty} \frac{1}{2T} \int_{-T}^{T} \left(\overline{H}_{m,n}^{(\ell)}(t - \Delta t)\right)^* \overline{H}_{l,i}^{(\ell)}(t) \, \mathrm{d}t \quad (27)$$

is the time-averaged ST-CCF between the ℓth sample functions of $\widetilde{H}_{m,n}(t)$ and $\widetilde{H}_{l,i}(t)$, denoted by $\overline{H}_{m,n}^{(\ell)}(t)$ and $\overline{H}_{l,i}^{(\ell)}(t)$, respectively [7]. Ergodicity enables the channel simulator to efficiently reproduce the channel correlation characteristics in each simulation run [7]. Nonetheless, the accuracy of the ergodic SOC-based simulators depends on a proper choice of the cisoids parameters. In particular, by comparing (9) and (11) with their counterparts in (23) and (25), we note that the set of parameters $\tilde{g}_k^{(m,n)}$, $\tilde{\Lambda}_{m,n}^{(k)}$ and $\tilde{v}_D^{(k)}$ in (20), should be computed aiming at maximizing the relationships

$$\widetilde{R}_{l,m,i,n}(\Delta t) \approx R_{l,m,i,n}(\Delta t), \quad |\Delta t| \leq T_{\max} \quad (28)$$

$$f_{\widetilde{Z}}(z) \approx f_Z(z), \quad z > 0 \quad (29)$$

for all $l, m \in \{1, 2, \ldots, M\}$ and $i, n \in \{1, 2, \ldots, N\}$, where $T_{\max}$ stands for the length of the time interval inside of which the approximation in (28) is of interest.

B. THE DRSM

An efficient solution to the parameter computation problem of the previous subsection is given by the RSM proposed in [21]. However, as noted in the introduction, a drawback of this PCM is that it was formulated by assuming ULAs and a particular 2D propagation scenario. The starting point toward the method's generalization w.r.t. 3D propagation and arbitrary antenna arrays is to express the surface integral in (11), which characterizes the ST-CCF of the reference channel model, as a double Riemann sum of the form:

$$R_{l,m,i,n}(\Delta t) \approx \sum_{k_\theta=1}^{K_\theta} \sum_{k_\phi=1}^{K_\phi} e^{j2\pi \Delta t \, \upsilon_D\left(\tilde{\theta}_R^{(k_\theta)}, \tilde{\phi}_R^{(k_\phi)}\right)}$$
$$\times e^{j2\pi \left[\Lambda_{l,i}\left(\tilde{\theta}_R^{(k_\theta)}, \tilde{\phi}_R^{(k_\phi)}\right) - \Lambda_{m,n}\left(\tilde{\theta}_R^{(k_\theta)}, \tilde{\phi}_R^{(k_\phi)}\right)\right]}$$
$$\times f_{\text{DOA}}^R\left(\tilde{\theta}_R^{(k_\theta)}, \tilde{\phi}_R^{(k_\phi)}\right) \Delta\theta \, \Delta\phi \qquad (30)$$

where $\Delta\theta = \pi/K_\theta$, $\Delta\phi = 2\pi/K_\phi$, and

$$\tilde{\theta}_R^{(k_\theta)} = \Delta\theta \, [k_\theta - 0.5], \quad k_\theta \in \{1, 2, \ldots, K_\theta\} \qquad (31)$$

$$\tilde{\phi}_R^{(k_\phi)} = \Delta\phi \, [k_\phi - 0.25], \quad k_\phi \in \{1, 2, \ldots, K_\phi\}. \qquad (32)$$

We note that the right-hand side of (30) asymptotically converges to the right-hand side of (11) in the limit when $K_\theta \to \infty$ and $K_\phi \to \infty$. An equivalence relationship can be established between (30) and (25) by expressing the double sum in (30) as a single sum over the ordered pairs in $\mathcal{R}_{\theta,\phi} = \left\{\tilde{\theta}_R^{(1)}, \tilde{\theta}_R^{(2)}, \ldots, \tilde{\theta}_R^{(K_\theta)}\right\} \otimes \left\{\tilde{\phi}_R^{(1)}, \tilde{\phi}_R^{(2)}, \ldots, \tilde{\phi}_R^{(K_\phi)}\right\}$, as follows

$$R_{l,m,i,n}(\Delta t) \approx \sum_{\eta \in \mathcal{R}_{\theta,\phi}} e^{j2\pi \Delta t \, \tilde{\upsilon}_D(\eta)} e^{j2\pi \left[\Lambda_{l,i}(\eta) - \Lambda_{m,n}(\eta)\right]}$$
$$\times f_{\text{DOA}}^R(\eta) \, \Delta\theta \, \Delta\phi \qquad (33)$$

$$\approx \sum_{k=1}^{K_\theta K_\phi} e^{j2\pi \Delta t \, \tilde{\upsilon}_D\left(\tilde{\theta}_R^{(k')}, \tilde{\phi}_R^{(k'')}\right)}$$
$$\times e^{j2\pi \left[\tilde{\Lambda}_{l,i}\left(\tilde{\theta}_R^{(k')}, \tilde{\phi}_R^{(k'')}\right) - \tilde{\Lambda}_{m,n}\left(\tilde{\theta}_R^{(k')}, \tilde{\phi}_R^{(k'')}\right)\right]}$$
$$\times f_{\text{DOA}}^R\left(\tilde{\theta}_R^{(k')}, \tilde{\phi}_R^{(k'')}\right) \Delta\theta \, \Delta\phi. \qquad (34)$$

where $k' = \lceil k/K_\theta \rceil$ and $k'' = k - K_\theta \lfloor (k-1)/K_\theta \rfloor$, for $k \in \{1, 2, \ldots, K_\theta K_\phi\}$. A comparison between (25) and (34) suggests that $\tilde{R}_{l,m,i,n}(\Delta t) \approx R_{l,m,i,n}(\Delta t)$, $|\Delta t| \leq T_{\max}$, if:

$$\tilde{\Lambda}_{m,n}^{(k)} = \Lambda_{m,n}\left(\tilde{\theta}_R^{(\lceil k/K_\theta \rceil)}, \tilde{\phi}_R^{(k-K_\theta \lfloor (k-1)/K_\theta \rfloor)}\right) \qquad (35)$$

$$\tilde{\upsilon}_D^{(k)} = \upsilon_D\left(\tilde{\theta}_R^{(\lceil k/K_\theta \rceil)}, \tilde{\phi}_R^{(k-K_\theta \lfloor (k-1)/K_\theta \rfloor)}\right) \qquad (36)$$

and

$$\tilde{g}_k = \sqrt{f_{\text{DOA}}^R\left(\tilde{\theta}_R^{(\lceil k/K_\theta \rceil)}, \tilde{\phi}_R^{(k-K_\theta \lfloor (k-1)/K_\theta \rfloor)}\right) \Delta\theta \, \Delta\phi} \qquad (37)$$

for $k = \{1, 2, \ldots, K_\theta \cdot K_\phi\}$, where $\Lambda_{m,n}$ and υ_D are given by (12) and (13).

The idea underlying the PCM in (35)–(37) is well suited for approximating the ST-CCF of the reference channel model. However, this idea does not guarantee a close approximation of the reference model's envelope PDF, $f_Z(z)$, because the cisoids' gains are not specified with the purpose of fitting (23) against the Rayleigh PDF in (9). In fact, the computation of $\tilde{g}_k$ according to (37) presents two important shortcomings. On the one hand, the gains are not normalized, meaning that the instantaneous average power, $\rho_{\tilde{H}}$, of the simulation model is not equal to one. This implies that the average power of the simulation model is different from that of the reference model. To avoid this problem, we redefine the gains as

$$\tilde{g}_k = \sqrt{\frac{f_{\text{DOA}}^R\left(\tilde{\theta}_R^{(\lceil k/K_\theta \rceil)}, \tilde{\phi}_R^{(k-K_\theta \lfloor (k-1)/K_\theta \rfloor)}\right)}{\sum_{i=1}^{K_\theta K_\phi} f_{\text{DOA}}^R\left(\tilde{\theta}_R^{(\lceil i/K_\theta \rceil)}, \tilde{\phi}_R^{(i-K_\theta \lfloor (i-1)/K_\theta \rfloor)}\right)}}. \qquad (38)$$

On the other hand, neither (37) nor (38) prevent the set of gains $\{\tilde{g}_k\}_{k=1}^{K_\theta K_\phi}$ to be mostly comprised of zeros, or near-zero elements, if the joint PDF of the DOA, $f_{\text{DOA}}^R(\tilde{\theta}_R, \tilde{\phi}_R)$, is densely concentrated around a particular DOA. This will result in a poor performance concerning the simulator's accuracy in approximating the envelope PDF of the reference model. This problem was originally noted in [20] for the case of single-input single-output (SISO) fixed-to-mobile (F2M) fading channels in 2D propagation environments. To bypass the problem, a threshold was considered in [20] to compute the cisoids' parameters only within the region of the DOA that produces meaningful values for $\tilde{g}_k$. For the simulation of our 3D reference channel model, the solution in [20] requires computing the deterministic angles $\tilde{\theta}_R^{(k_\theta)}$ and $\tilde{\phi}_R^{(k_\phi)}$ by considering the subregion

$$\mathcal{S}_{\theta,\phi} = \left\{(\theta, \phi) \,\middle|\, \theta \in [0, \pi), \phi \in [0, 2\pi), f_{\text{DOA}}^R(\theta, \phi) \geq \Gamma\right\} \qquad (39)$$

where $\Gamma \in (0, \sup\{f_{\text{DOA}}^R(\theta, \phi)\})$ is a given threshold. To avoid the complications of identifying the contour of the subregion of interest, we assume that $f_{\text{DOA}}^R(\theta, \phi)$ is a monomodal PDF, so that the condition in (39) can be restated w.r.t. the subintervals

$$\mathcal{I}_\theta = [\theta_{\min}, \theta_{\max}] = \left\{\theta \in [0, \pi) \,\middle|\, f_\Theta^R(\theta) \geq \Gamma_\theta\right\} \qquad (40a)$$

$$\mathcal{I}_\phi = [\phi_{\min}, \phi_{\max}] = \left\{\phi \in [\mu_\phi - \pi, \mu_\phi + \pi) \,\middle|\, f_\Phi^R(\phi) \geq \Gamma_\phi\right\} \qquad (40b)$$

where $f_\Theta^R(\theta)$ and $f_\Phi^R(\phi)$ are the marginal PDFs of the IAOA, θ_R, and AAOA, ϕ_T, respectively, μ_θ is the mean AAOA, whereas $\Gamma_\theta \in (0, \sup\{f_\Theta^R(\theta)\})$ and $\Gamma_\phi \in (0, \sup\{f_\Phi^R(\phi)\})$. The assumption of a monomodal joint-PDF of the DOA is necessary to ensure that exactly one subinterval can be identified both in $[0, \pi)$ and $[\mu - \pi, \mu + \pi)$ satisfying (40). While restrictive, this assumption is in line with the characteristics of several monomodal parametric models for the DOA (DOD) statistics that are widely used in the literature, such as those surveyed in [30]. Following [20], we determine the thresholds

Γ_θ and Γ_ϕ in accordance to the rule-of-thumb:

$$\Gamma_\theta = \sup\left\{f_\Theta^R(\theta)\right\}\frac{\eta}{100} \tag{41a}$$

$$\Gamma_\phi = \sup\left\{f_\Phi^R(\phi)\right\}\frac{\eta}{100} \tag{41b}$$

where $\eta \in [0.1, 1]$. The deterministic angles $\tilde{\theta}_R^{(k_\theta)}$ and $\tilde{\phi}_R^{(k_\theta)}$ can be computed as

$$\tilde{\theta}_R^{(k)} = \theta_{\min} + \left(\left\lceil\frac{k}{K_\phi}\right\rceil - \frac{1}{2}\right)\Delta\theta \tag{42}$$

$$\tilde{\phi}_R^{(k)} = \phi_{\min} + \left(k - K_\phi\left\lfloor\frac{k-1}{K_\phi}\right\rfloor - \frac{1}{4}\right)\Delta\phi \tag{43}$$

for $k \in \{1, 2, \ldots, K_\theta \cdot K_\phi\}$, where

$$\Delta\theta = \frac{\theta_{\max} - \theta_{\min}}{K_\theta} \tag{44}$$

$$\Delta\phi = \frac{\phi_{\max} - \phi_{\min}}{K_\phi}. \tag{45}$$

The boundaries of $\mathcal{I}_\theta = [\theta_{\min}, \theta_{\max}]$ and $\mathcal{I}_\phi = [\phi_{\min}, \phi_{\max}]$ can easily be computed either numerically or analytically, once the monomodal marginal PDFs $f_\Theta^R(\theta)$ and $f_\Phi^R(\phi)$ are known. Equations (20), (35), (36), (38), (42) and (43) summarize the methodology of the DRSM. A pseudo-code for the implementation of this PCM is presented in Algorithm 1.

IV. THE RRSM FOR THE SOC-BASED SIMULATION OF 3D NARROWBAND MIMO M2M CHANNELS

The DRSM has been conceived specifically for the ergodic SOC-based simulation of 3D MIMO channels. Ergodicity is a desirable property for the reasons stated in the previous section. It should be noted, nonetheless, that this property relies on the generation of channel waveforms having a long length in time (infinitely long in theory, and at least in the order of a few tens of seconds in practice [18], [34]). The fulfillment of this condition is impractical for the simulation of fading channels characterized by short stationary time intervals, such as the short-range vehicle-to-vehicle (V2V) radio communications channel [35]. However, the simulation of fading channels having short stationary time intervals can be accomplished by means of a non-ergodic stationary SOC-based simulator, as the performance of this type of simulators does not depend on the length of the generated channel waveforms, but on the form of its ensemble averages.

A. THE NON-ERGODIC STATIONARY SOC-BASED SIMULATION MODEL

For the generalization of the original RSM w.r.t. the non-ergodic stationary simulation of 3D MIMO M2M fading channels, we assume that the parameters of the SOC-based simulation in (20) are all modeled by random variables. Moreover, we assume that all the cisoids parameters are inter-path independent random variables, meaning that the set $\left\{\tilde{g}_k, \tilde{\psi}_k, \tilde{\Lambda}_{m,n}^{(k)}, \tilde{\upsilon}_D^{(k)}\right\}$ is comprised of random variables which are statistically independent from those in

---

Algorithm 1: Pseudo-Code for the DRSM.

Input: $M, N, \lambda, \mathbf{d}_T, \mathbf{d}_R, \mathbf{v}_T, \mathbf{v}_R,$
$\left[\mathbf{a}_T^{(1)}, \mathbf{a}_T^{(2)}, \ldots \mathbf{a}_T^{(N)}\right], \left[\mathbf{a}_R^{(1)}, \mathbf{a}_R^{(2)}, \ldots \mathbf{a}_R^{(M)}\right], K_\theta, K_\phi, \eta,$
$f_{\text{DOA}}^R(\theta_R, \phi_R), \mathcal{G}(\theta_R, \phi_R).$
Output: $\tilde{\mathbf{g}} \in \mathbb{R}^{K \times 1}, \tilde{\boldsymbol{\upsilon}}_D \in \mathbb{R}^{K \times 1}, \tilde{\boldsymbol{\Omega}} \in \mathbb{R}^{M \times N \cdot K}$

1: Find $\theta_{\min}$ and $\theta_{\max}$.
2: Find $\phi_{\min}$ and $\phi_{\max}$.
3: Compute $\Delta\theta$: Evaluate (44)
4: Compute $\Delta\phi$: Evaluate (45)
5: $K \leftarrow K_\theta \cdot K_\phi$
6: $\mathbf{d}_{TR} \leftarrow \mathbf{d}_R - \mathbf{d}_T$
7: $\rho \leftarrow 0$
8: **for** $k = 1$ to K **do**
9:      Compute $\tilde{\theta}_R^{(k)}$: Evaluate (42)
10:      Compute $\tilde{\phi}_R^{(k)}$: Evaluate (43)
11:      Compute $\tilde{g}_k$: Evaluate (37)
12:      $\rho \leftarrow \rho + \tilde{g}_k^2$
13:      Compute $\tilde{\upsilon}_D^{(k)}$: Evaluate (36), (12), (16) and (17)
14:      **for** $m = 1$ to M **do**
15:          **for** $n = 1$ to N **do**
16:              Compute $\tilde{\Lambda}_{m,n}^{(k)}$: Evaluate (35), (13), (16) and (17)
17:          **end for**
18:      **end for**
19:      $\tilde{\boldsymbol{\Omega}}_k \leftarrow \begin{bmatrix} \tilde{\Lambda}_{1,1}^{(k)} & \tilde{\Lambda}_{1,2}^{(k)} & \cdots & \tilde{\Lambda}_{1,N}^{(k)} \\ \tilde{\Lambda}_{2,1}^{(k)} & \tilde{\Lambda}_{2,2}^{(k)} & \cdots & \tilde{\Lambda}_{2,N}^{(k)} \\ \vdots & \vdots & \ddots & \vdots \\ \tilde{\Lambda}_{M,1}^{(k)} & \tilde{\Lambda}_{N,2}^{(k)} & \cdots & \tilde{\Lambda}_{M,N}^{(k)} \end{bmatrix}$
20: **end for**
21: $\tilde{\mathbf{g}} \leftarrow [\tilde{g}_1, \tilde{g}_2, \ldots \tilde{g}_K]^\top / \sqrt{\rho}$
22: $\tilde{\boldsymbol{\upsilon}}_D \leftarrow [\tilde{\upsilon}_1, \tilde{\upsilon}_2, \ldots \tilde{\upsilon}_K]^\top$
23: $\tilde{\boldsymbol{\Omega}} \leftarrow [\tilde{\boldsymbol{\Omega}}_1, \tilde{\boldsymbol{\Omega}}_2, \ldots \tilde{\boldsymbol{\Omega}}_K]$

$\left\{\tilde{g}_l, \tilde{\psi}_l, \tilde{\Lambda}_{m,n}^{(l)}, \tilde{\upsilon}_D^{(l)}\right\}$, for $k \neq l$. However, only the phases, $\tilde{\psi}_k$, are assumed to be intra-path independent, i.e., $\tilde{\psi}_k$ is statistically independent from $\tilde{g}_k$, $\tilde{\Lambda}_{m,n}^{(k)}$, and $\tilde{\upsilon}_D^{(k)}$, $\forall k \in \{1, 2, \ldots, K\}$, $m \in \{1, 2, \ldots, M\}$, $n \in \{1, 2, \ldots, N\}$, whereas the latter three parameters are not necessarily mutually statistically independent. We further assume that the phase shifts, $\tilde{\psi}_k$, are uniformly distributed in $[0, 2\pi)$. Under these assumptions, it can be verified that the mean value, the instantaneous power, the FO envelope PDF, and the FO phase PDF of $\tilde{H}_{m,n}(t)$ are equal to:

$$\mu_{\tilde{H}}(t) \triangleq \mathcal{E}\left\{\tilde{H}_{m,n}(t)\right\} = 0 \tag{46}$$

$$\rho_{\tilde{H}}(t) \triangleq \mathcal{E}\left\{|\tilde{H}_{m,n}(t)|^2\right\} = \sum_{k=1}^{K}\mathcal{E}\{\tilde{g}_k^2\} \tag{47}$$

$$f_{\tilde{Z}}(z; t) = z(2\pi)^2\int_0^\infty\left[\prod_{k=1}^{K}\int_0^\infty f_{\tilde{g}}^{(k)}(\xi_k)J_0(2\pi\xi_k x)\,\mathrm{d}\xi_k\right]$$
$$\times J_0(2\pi zx)x\,\mathrm{d}x, \quad z \geq 0 \tag{48}$$

$$f_{\tilde{\Psi}}(\psi; t) = \frac{1}{2\pi}, \quad \psi \in [0, 2\pi) \tag{49}$$

where $f_{\tilde{g}}^{(k)}(\xi)$ stands for the PDF of the amplitude, $\tilde{g}_k$, of the kth cisoid [12]. Likewise, it can be shown that the ST-CCF between $\widetilde{H}_{m,n}(t)$ and $\widetilde{H}_{l,i}(t)$ is equal to

$$\widetilde{R}_{l,m,i,n}(\Delta t) \triangleq \mathcal{E}\left\{\widetilde{H}_{m,n}^*(t - \Delta t)\widetilde{H}_{l,i}(t)\right\}$$

$$= \sum_{k=1}^{K} \mathcal{E}\left\{\tilde{g}_k^2 e^{j2\pi\left[\tilde{\Lambda}_{l,i}^{(k)} - \tilde{\Lambda}_{m,n}^{(k)} + \Delta t \tilde{v}_D^{(k)}\right]}\right\}. \tag{50}$$

B. THE RRSM

The problem at hand consists in finding the random variables $\tilde{g}_k$, $\tilde{\Lambda}_{m,n}^{(k)}$ and $\tilde{v}_D^{(k)}$ such that:

$$\rho_{\widetilde{H}} = \rho_H = 1 \tag{51}$$

$$\widetilde{R}_{l,m,i,n}(\Delta t) \approx R_{l,m,i,n}(\Delta t), \quad |\Delta t| \leq T_{\max} \tag{52}$$

$$f_{\tilde{Z}}(z) \approx f_Z(z), \quad z > 0. \tag{53}$$

A simple, yet effective solution to this random parameter computation method can be obtained by reformulating the DRSM from a stochastic perspective. Specifically, and by assuming again that the DOA statistics follow a monomodal joint PDF, we define:

$$\tilde{g}_k = \sqrt{\frac{f_{\text{DOA}}^R\left(\tilde{\theta}_R^{(k)}, \tilde{\phi}_R^{(k)}\right) \Delta_\theta \Delta_\phi}{\int_{\theta_{\min}}^{\theta_{\max}} \int_{\phi_{\min}}^{\phi_{\max}} f_{\text{DOA}}^R(\theta_R, \phi_R) \, d\theta_R \, d\phi_R}} \tag{54}$$

$$\tilde{\Lambda}_{m,n}^{(k)} = \Lambda_{m,n}^{(k)}\left(\tilde{\theta}_R^{(k)}, \tilde{\phi}_R^{(k)}\right) \tag{55}$$

$$\tilde{v}_D^{(k)} = v_D^{(k)}\left(\tilde{\theta}_R^{(k)}, \tilde{\phi}_R^{(k)}\right) \tag{56}$$

where the IAOAs, $\tilde{\theta}_R^{(k)}$, and the AAOAs, $\tilde{\phi}_R^{(k)}$, are given as:

$$\tilde{\theta}_R^{(k)} = \vartheta_k + \left(\left\lceil\frac{k}{K_\phi}\right\rceil - 1\right)\Delta\theta \tag{57}$$

$$\tilde{\phi}_R^{(k)} = \varphi_k + \left(k - K_\phi\left\lfloor\frac{k-1}{K_\phi}\right\rfloor - 1\right)\Delta\phi. \tag{58}$$

The angles ϑ_k are i.i.d. random variables, each characterized by a uniform distribution in $[\theta_{\min}, \theta_{\min} + \Delta\theta)$. The angles φ_k are also modeled by i.i.d. random variables having a uniform distribution in $[\phi_{\min}, \phi_{\min} + \Delta\phi)$. Equations (54)–(58) constitute the RRSM. Algorithm 2 presents a pseudo-code for the implementation of this PCM.

Some important remarks about the RRSM are in order. First, we note that if the parameters of the non-ergodic WSS SOC-based simulation model are computed in accordance to the RRSM, then:

$$\rho_{\widetilde{H}} = 1 \tag{59}$$

$$\widetilde{R}_{l,m,i,n}(\Delta t) = \frac{1}{\int_{\theta_{\min}}^{\theta_{\max}} \int_{\phi_{\min}}^{\phi_{\max}} f_{\text{DOA}}^R(x, y) \, dx \, dy}$$

$$\times \int_{\theta_{\min}}^{\theta_{\max}} \int_{\phi_{\min}}^{\phi_{\max}} e^{j2\pi \Delta t \, v_D(\theta_R, \phi_R)}$$

Algorithm 2: Pseudo-Code for the RRSM.

Input: M, N, λ, $\mathbf{d}_T$, $\mathbf{d}_R$, $\mathbf{v}_T$, $\mathbf{v}_R$,
$\left[\mathbf{a}_T^{(1)}, \mathbf{a}_T^{(2)}, \ldots \mathbf{a}_T^{(N)}\right]$, $\left[\mathbf{a}_R^{(1)}, \mathbf{a}_R^{(2)}, \ldots \mathbf{a}_R^{(M)}\right]$, K_θ, K_ϕ, η,
$f_{\text{DOA}}^R(\theta_R, \phi_R)$,
$\mathcal{G}(\theta_R, \phi_R)$.
Output: $\tilde{\mathbf{g}} \in \mathbb{R}^{K \times 1}$, $\tilde{\boldsymbol{v}}_D \in \mathbb{R}^{K \times 1}$, $\tilde{\boldsymbol{\Omega}} \in \mathbb{R}^{M \times N \cdot K}$

1: Find $\theta_{\min}$ and $\theta_{\max}$.
2: Find $\phi_{\min}$ and $\phi_{\max}$.
3: Compute $\Delta\theta$: Evaluate (44)
4: Compute $\Delta\phi$: Evaluate (45)
5: $K \leftarrow K_\theta \cdot K_\phi$
6: $\mathbf{d}_{TR} \leftarrow \mathbf{d}_R - \mathbf{d}_T$
7: $\rho \leftarrow \int_{\theta_{\min}}^{\theta_{\max}} \int_{\phi_{\min}}^{\phi_{\max}} f_{\text{DOA}}^R(\theta_R, \phi_R) \, d\theta_R \, d\phi_R$
8: **for** $k = 1$ to K **do**
9:    Compute $\vartheta_R^{(k)}$: Generate a random number uniformly distributed in $[\theta_{\min}, \theta_{\min} + \Delta\theta)$
10:   Compute $\varphi_R^{(k)}$: Generate a random number uniformly distributed in $[\phi_{\min}, \phi_{\min} + \Delta\phi)$
11:   Compute $\tilde{\theta}_R^{(k)}$: Evaluate (57)
12:   Compute $\tilde{\phi}_R^{(k)}$: Evaluate (58)
13:   Compute $\tilde{g}_k$: Evaluate (54)
14:   Compute $\tilde{v}_D^{(k)}$: Evaluate (56), (12), (16) and (17)
15:   **for** $m = 1$ to M **do**
16:     **for** $n = 1$ to N **do**
17:       Compute $\tilde{\Lambda}_{m,n}^{(k)}$: Evaluate (55), (13), (16) and (17)
18:     **end for**
19:   **end for**
20:   $\tilde{\boldsymbol{\Omega}}_k \leftarrow \begin{bmatrix} \tilde{\Lambda}_{1,1}^{(k)} & \tilde{\Lambda}_{1,2}^{(k)} & \cdots & \tilde{\Lambda}_{1,N}^{(k)} \\ \tilde{\Lambda}_{2,1}^{(k)} & \tilde{\Lambda}_{2,2}^{(k)} & \cdots & \tilde{\Lambda}_{2,N}^{(k)} \\ \vdots & \vdots & \ddots & \vdots \\ \tilde{\Lambda}_{M,1}^{(k)} & \tilde{\Lambda}_{N,2}^{(k)} & \cdots & \tilde{\Lambda}_{M,N}^{(k)} \end{bmatrix}$
21: **end for**
22: $\tilde{\mathbf{g}} \leftarrow [\tilde{g}_1, \tilde{g}_2, \ldots \tilde{g}_K]^\top$
23: $\tilde{\boldsymbol{v}}_D \leftarrow [\tilde{v}_1, \tilde{v}_2, \ldots \tilde{v}_K]^\top$
24: $\tilde{\boldsymbol{\Omega}} \leftarrow [\tilde{\boldsymbol{\Omega}}_1, \tilde{\boldsymbol{\Omega}}_2, \ldots \tilde{\boldsymbol{\Omega}}_K]$

$$\times \, e^{j2\pi\left[\Lambda_{l,i}(\theta_R, \phi_R) - \Lambda_{m,n}(\theta_R, \phi_R)\right]}$$

$$\times f_{\text{DOA}}^R(\theta_R, \phi_R) \, d\theta_R \, d\phi_R. \tag{60}$$

These results are valid for any number of cisoids, i.e., for any $K \in \mathbb{Z}_+$. From (60) and (11), it follows that the RRSM provides an exact fitting to the reference channel model's ST-CCF if $\theta_{\min} = \phi_{\min} = 0$, $\theta_{\max} = \pi$ and $\phi_{\max} = 2\pi$. In this regard, the RRSM performs the same as the direct Monte Carlo method (MCM) [7]. This is not surprising, since the RRSM is inspired by the concepts of Monte Carlo integration [36]. However, the MCM computes the parameters of the non-ergodic stationary SOC-based simulation model by relying on the implementation of intricate random number generators that diminish the simulator's flexibility, as discussed at the

end of Section II. In contrast, the RRSM favors the simulator's reconfigurability by computing the IAOAs, $\tilde{\theta}_R^{(k)}$, and the AAOAs, $\tilde{\phi}_R^{(k)}$, through the straightforward transformations of uniform random variables given by (57) and (58).

Another difference between the MCM and the RRSM is that the former method defines the IAOAs and the AAOAs by considering an indiscriminate sampling of the DOA's range, such that $\tilde{\theta}_R^{(k)} \in [0, \pi)$ and $\tilde{\phi}_R^{(k)} \in [0, 2\pi)$, for $k \in \{1, 2, \ldots, K\}$. In contrast, the RRSM considers a stratified sampling, where:

$$\tilde{\theta}_R^{(k)} \in \left[\theta_{\min} + \left(\left\lceil \frac{k}{K_\phi} \right\rceil - 1 \right) \Delta_\theta, \theta_{\min} + \left\lceil \frac{k}{K_\phi} \right\rceil \Delta_\theta \right) \quad (61)$$

$$\tilde{\phi}_R^{(k)} \in \left[\phi_{\min} + \left(k - K_\phi \left\lfloor \frac{k-1}{K_\phi} \right\rfloor - 1 \right) \Delta_\phi, \right.$$

$$\left. \phi_{\min} + \left(k - K_\phi \left\lfloor \frac{k-1}{K_\phi} \right\rfloor \right) \Delta_\phi \right) \quad (62)$$

for $k \in \{1, 2, \ldots, K\}$. As a result of this stratification, the ordered pairs of random IAOAs and AAOAs, $(\tilde{\theta}_R^{(k)}, \tilde{\phi}_R^{(k)})$, that are drawn in each simulation run are more evenly distributed over the DOA's range as compared to those pairs produced by the MCM. A more homogeneous sampling is convenient [36], as it allows to reduce the number, $L \in \mathbb{Z}_+$, of realizations required by the non-ergodic simulator to provide a close approximation to the reference model's ST-CCF. In other words, a more homogeneous sampling allows to reduce the value of L for which

$$\frac{1}{L} \sum_{\ell=1}^{L} \overline{R}_{l,m,i,n}^{(\ell)}(\Delta t) \approx \widetilde{R}_{l,m,i,n}(\Delta t) \approx R_{l,m,i,n}(\Delta t) \quad (63)$$

where $\overline{R}_{l,m,i,n}^{(\ell)}(\Delta t)$ denotes the time-averaged ST-CCF between the ℓth sample functions of $\widetilde{H}_{m,n}^*(t)$ and $\widetilde{H}_{l,i}(t)$ (see (27)). The idea of partitioning the DOA's range was originally proposed in [37] for the particular case of the SOS-based simulation of 2D F2M SISO channels and assuming isotropic scattering conditions. The RRSM extends such an idea w.r.t. the simulation of 3D MIMO M2M channels and arbitrary scattering conditions.

Finally, from (60) and (11), we can also observe that if $0 < \theta_{\min} < \theta_{\max} < \pi$, and $0 < \phi_{\min} < \phi_{\max} < 2\pi$, then the RRSM provides just an approximation to the reference model's ST-CCF. While sampling the DOA's range over such a shortened region is in detriment of the simulator's capacity to exactly reproduce $R_{l,m,i,n}(\Delta t)$, this strategy proves convenient to improve the simulator's efficiency concerning the emulation of the reference model's envelope PDF due to the same reasons stated in the previous section for the case of the DRSM.

V. SIMULATION EXAMPLES
A. CONSIDERATIONS
This section presents several simulation examples that illustrate the performance of the DRSM and the RRSM. For that

purpose, we consider six different simulation cases resulting from the pairing of the sphere and cylinder geometrical scattering models with the ULA, UCA and URA antenna array configurations (the same type of antenna array is assumed to be employed at both the T_X and the R_X). We assumed a narrowband MIMO M2M communications system having a central frequency $f_c = 2.5$ GHz ($\lambda \approx 0.12$), $N = 10$ transmitting antennas, and $M = 9$ receiving antennas. The initial position of the T_X was chosen equal to $\mathbf{d}_T = 1.8\hat{\mathbf{z}}$ [m], whereas that of the R_X was equal to $\mathbf{d}_R = 800\hat{\mathbf{x}} + 2\hat{\mathbf{z}}$ [m]. The velocity vector of the T_X and the R_X are given in spherical coordinates as $\mathbf{v}_T = (13.9, 80°, 350°)$ [m/s] and $\mathbf{v}_R = (13.9, 90°, 170°)$ [m/s]. The function $\mathcal{G}(\theta_R, \phi_R)$, which characterizes the geometrical configuration of the propagation area, is defined in accordance with (93) and (94) for the sphere and cylinder geometrical models, respectively. For both scattering models, we considered the same radius $R = 50$ [m] of the sphere and cylinder. For the cylinder model, we also chose a height $h_{\text{cyl}} = 25$ [m]. The position of the antenna elements w.r.t. the array's center was set according to (90), where the basic antenna element position vectors were set following (84), (86), and (88). The distance between adjacent array elements was equal to 0.5 wavelengths for the three array configurations ($\Delta_A = \Delta_x = \Delta_y = \lambda/2$). Table 1 shows the orientation and rotation angles assumed for the transmitting and receiving antenna arrays. For the URA configuration, we chose $N_x = 5$ and $N_y = 2$ ($N_x \cdot N_y = N = 10$), whereas $M_x = 3$ and $M_y = 3$ ($M_x \cdot M_y = M = 9$).

The applicability of the DRSM and the RRSM is not restricted to a particular form of the joint PDF of the DOA. However, to demonstrate the flexibility of the DRSM and RRSM, we assumed that the IAOA, θ_R, and the AAOA, ϕ_R, are jointly characterized by the VMF distribution [30]

$$f_{\text{DOA}}^R(\theta_R, \phi_R) = \frac{\kappa}{4\pi \sinh(\kappa)} \sin(\theta_R)$$

$$\times \exp\{\kappa \left[\cos(\theta_R)\cos(\mu_\theta)\right.$$

$$\left. + \sin(\theta_R)\sin(\mu_\theta)\cos(\phi_R - \mu_\phi)\right]\} \quad (64)$$

where $\kappa \geq 0$ is a concentration parameter, μ_θ and μ_ϕ stand for the mean IAOA and mean AAOA, respectively, $\sinh(\cdot)$ is the hyperbolic sine function, and $I_0(\cdot)$ is the modified Bessel function of order zero. For the parameters of these joint-PDFs, we considered $k = 5$, $\mu_\theta = \pi/2$, and $\mu_\phi = 0$.[3]

Concerning the computation of the simulation model's IAOAs and AAOAs ($\tilde{\theta}_R^{(k)}$ and $\tilde{\phi}_R^{(k)}$), we considered a partition of the relevant range of the IAOA, $[\theta_{\min}, \theta_{\max}]$, comprising $K_\theta = 6$ subintervals (number of cisoids in the IAOA domain), whereas we partitioned the AAOA's range, $[\phi_{\min}, \phi_{\max}]$, into $K_\phi = 30$ subintervals (number of cisoids in the AAOA domain). The thresholds Γ_θ and Γ_ϕ were computed following (41) with $\eta = 1$.

---

[3]The reader is referred to [25] for additional results obtained for the DRSM by assuming that θ_R and ϕ_R are mutually statistically independent and characterized by the circular von-Mises [38] and circular Laplacian [39] PDFs, respectively.

TABLE 1. Orientation and Rotation of the Three Antenna Array Configurations

Array configuration	θ_{arr}^T	θ_{arr}^T	ξ_{arr}^T	θ_{arr}^R	θ_{arr}^R	ξ_{arr}^R
ULA	90°	90°	0°	90°	90°	0°
UCA	90°	0°	0°	90°	0°	0°
URA	90°	0°	0°	90°	0°	0°

To evaluate the performance of the DRSM and the RRSM w.r.t. the emulation of the correlation properties of the reference MIMO channel model, we consider the accuracy of these PCMs in approximating the TACF

$$R(\Delta t) \triangleq \mathcal{E}\{H_{m,n}^*(t - \Delta t)H_{m,n}(t)\} \tag{65}$$

for $\Delta t \in \mathbb{R}$, $n \in \{1, 2, \ldots, N\}$, and $m \in \{1, 2, \ldots, M\}$, as well as the space-cross-correlation matrix (SCCM)

$$\mathbf{R} \triangleq \mathcal{E}\left\{\mathbf{h}^* \mathbf{h}^\top\right\} \tag{66}$$

where

$$\mathbf{h} = \text{vec}\left\{\mathbf{H}(t)\big|_{t=0}\right\} \tag{67}$$

$$\mathbf{H}(t) = \begin{bmatrix} H_{1,1}(t) & H_{1,2}(t) & \ldots & H_{1,N}(t) \\ H_{2,1}(t) & H_{2,2}(t) & \ldots & H_{2,N}(t) \\ \vdots & \vdots & \ddots & \vdots \\ H_{M,1}(t) & H_{M,2}(t) & \ldots & H_{M,N}(t) \end{bmatrix}. \tag{68}$$

It is worth noting that

$$\mathbf{R} = \begin{bmatrix} \mathbf{R}_{1,1}^{R_X} & \mathbf{R}_{1,2}^{R_X} & \ldots & \mathbf{R}_{1,N}^{R_X} \\ \mathbf{R}_{2,1}^{R_X} & \mathbf{R}_{2,2}^{R_X} & \ldots & \mathbf{R}_{2,N}^{R_X} \\ \vdots & \vdots & \ddots & \vdots \\ \mathbf{R}_{N,1}^{R_X} & \mathbf{R}_{N,2}^{R_X} & \ldots & \mathbf{R}_{N,N}^{R_X} \end{bmatrix} \tag{69}$$

where the submatrix $\mathbf{R}_{n,i}^{R_X} \in \mathbb{C}^{M \times M}$ characterizes the cross-correlation between receiving antennas for the pair of the nth and ith transmitting antennas. This matrix is given as

$$\mathbf{R}_{n,i}^{R_X} \triangleq \mathcal{E}\left\{\mathbf{h}_n^* \mathbf{h}_i^\top\right\}, \quad n, i \in \{1, 2, \ldots, N\} \tag{70}$$

where $\mathbf{h}_n \in \mathbb{C}^{M \times 1}$ stands for the nth column of $\mathbf{H}(0)$, i.e.,

$$\mathbf{h}_n = \begin{bmatrix} H_{1,n}(0) & H_{2,n}(0) & \ldots & H_{M,n}(0) \end{bmatrix}^\top. \tag{71}$$

The SCCM, $\mathbf{R}$, and the $N \cdot N$ space-cross-correlation submatrices (SCCS), $\mathbf{R}_{n,i}^{R_X}$, are Hermitian matrices as a result of the wide-sense stationarity of the reference channel model. However, for the SCCS, and depending on the arrays' geometry, we have that in general

$$\mathbf{R}_{n,i}^{R_X} \neq \mathbf{R}_{n',i'}^{R_X}, \quad \text{if either } n \neq n' \text{ or } i \neq i'. \tag{72}$$

In turn, we define the SCCM of the SOC-based simulation model as

$$\widetilde{\mathbf{R}} \triangleq \mathcal{E}\left\{\widetilde{\mathbf{h}}^* \widetilde{\mathbf{h}}^\top\right\} \tag{73}$$

where

$$\widetilde{\mathbf{h}} = \text{vec}\left\{\widetilde{\mathbf{H}}(t)\big|_{t=0}\right\} \tag{74}$$

and

$$\widetilde{\mathbf{H}}(t) = \begin{bmatrix} \widetilde{H}_{1,1}(t) & \widetilde{H}_{1,2}(t) & \ldots & \widetilde{H}_{1,N}(t) \\ \widetilde{H}_{2,1}(t) & \widetilde{H}_{2,2}(t) & \ldots & \widetilde{H}_{2,N}(t) \\ \vdots & \vdots & \ddots & \vdots \\ \widetilde{H}_{M,1}(t) & \widetilde{H}_{M,2}(t) & \ldots & \widetilde{H}_{M,N}(t) \end{bmatrix} \tag{75}$$

is the matrix of the complex-valued MIMO channel waveforms produced by the simulator. As in the case of $\mathbf{R}$, the simulation model's SCCM can be written as

$$\widetilde{\mathbf{R}} = \begin{bmatrix} \widetilde{\mathbf{R}}_{1,1}^{R_X} & \widetilde{\mathbf{R}}_{1,2}^{R_X} & \ldots & \widetilde{\mathbf{R}}_{1,N}^{R_X} \\ \widetilde{\mathbf{R}}_{2,1}^{R_X} & \widetilde{\mathbf{R}}_{2,2}^{R_X} & \ldots & \widetilde{\mathbf{R}}_{2,N}^{R_X} \\ \vdots & \vdots & \ddots & \vdots \\ \widetilde{\mathbf{R}}_{N,1}^{R_X} & \widetilde{\mathbf{R}}_{N,2}^{R_X} & \ldots & \widetilde{\mathbf{R}}_{N,N}^{R_X} \end{bmatrix} \tag{76}$$

where

$$\widetilde{\mathbf{R}}_{n,i}^{R_X} \triangleq \mathcal{E}\left\{\widetilde{\mathbf{h}}_n^* \widetilde{\mathbf{h}}_i^\top\right\}, \quad n, i \in \{1, 2, \ldots, N\} \tag{77}$$

and

$$\widetilde{\mathbf{h}}_n = \begin{bmatrix} \widetilde{H}_{1,n}(0) & \widetilde{H}_{2,n}(0) & \ldots & \widetilde{H}_{M,n}(0) \end{bmatrix}^\top. \tag{78}$$

B. EXAMPLES OF THE GENERATED MIMO CHANNEL WAVEFORMS

Fig. 2 shows six line graphs of the envelope of $N \cdot M = 90$ MIMO channel waveforms generated by applying the DRSM and the RRSM for $t \in [0, 16]$ [ms], the sphere scattering model, and the three antenna array configurations.[4] The six sets of waveforms presented in this figure were generated by considering the same outcomes of the $K = K_\theta K_\phi = 180$ random phase shifts, $\widetilde{\psi}_k$. For the case of the RRSM, we also considered the same outcomes of the random IAOAs, ϑ_k, and AAOAs, φ_k, in (57) and (58). Therefore, the differences among the waveforms in Fig. 2(a), (c), and (e), as well as among those in Fig 2(b), (d), and (f), stem entirely from the array configuration. We also note that the slight differences between the waveforms produced by the DRSM and RRSM are due to the randomness of this latter method's IAOAs, $\widetilde{\theta}_R^{(k)}$, and AAOAs, $\widetilde{\phi}_R^{(k)}$.

The envelope curves in Fig. 2 exhibit the deep and abrupt fades that are characteristic of small-scale mobile fading channels. Moreover, the correlation in time and space between MIMO subchannels, which is determined by the geometrical configuration of the propagation environment and the antenna arrays, is also noticeable from these graphs. In fact, the correlation between envelope curves appears to be higher for the UCA and URA than for the ULA, which is in line with the geometry of these three antenna arrays. To make these observations more evident, we present in Fig. 3 the heatmaps

---

[4]Examples of the envelope curves obtained for the cylinder scattering model are not presented here for reasons of brevity

(a) DRSM & ULAs.

(b) RRSM & ULAs.

(c) DRSM & UCAs.

(d) RRSM & UCAs.

(e) DRSM & URAs.

(f) RRSM & URAs.
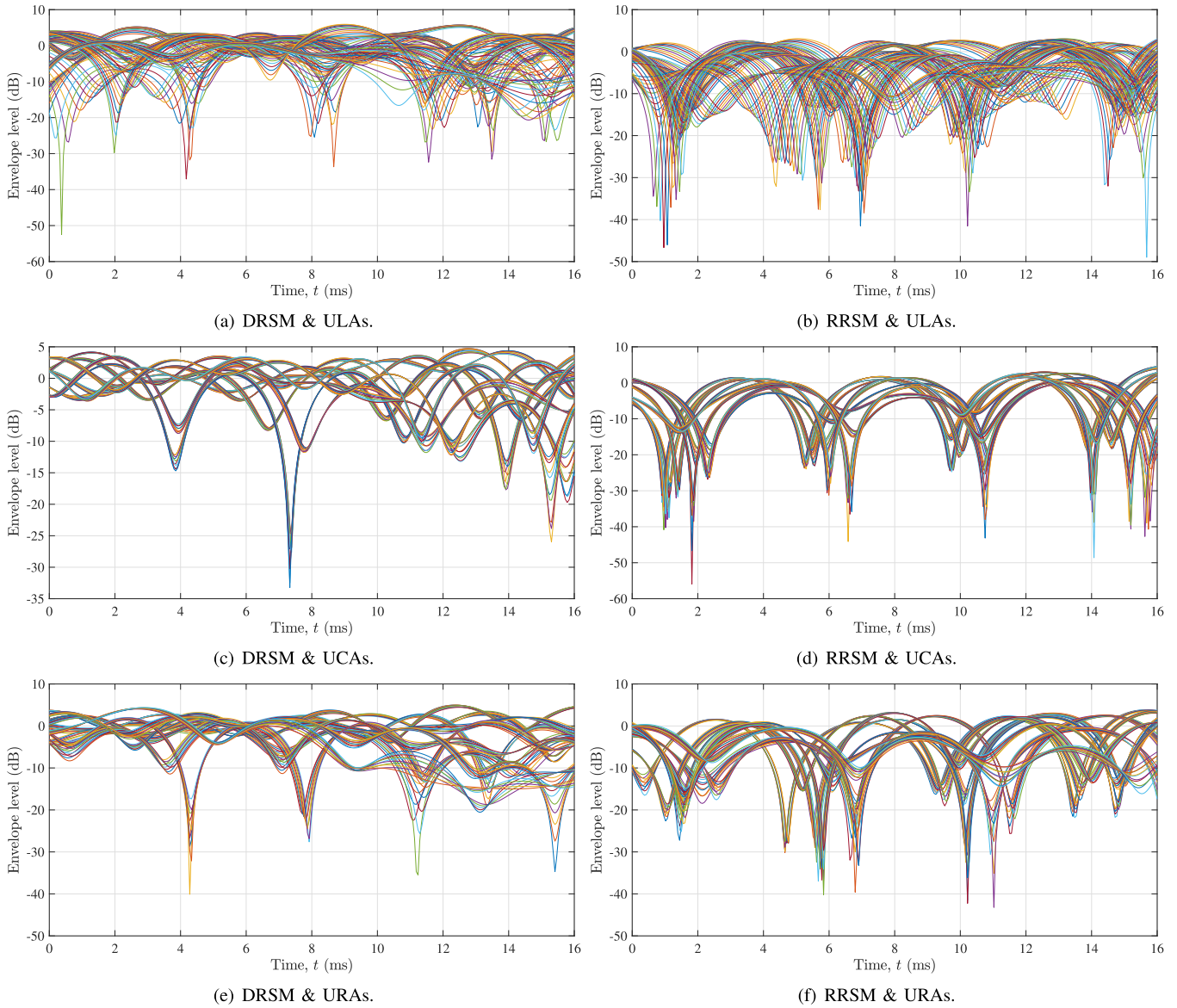
FIGURE 2. Line plot of the envelope of the MIMO channel waveforms generated by the SOC-based simulation model for the DRSM, the RRSM, the sphere scattering model, ULAs ($N = 10$, $M = 8$, $\theta_{arr}^T = 90°$, $\phi_{arr}^T = 90°$, $\chi_{arr}^T = 0°$, $\theta_{arr}^R = 90°$, $\phi_{arr}^R = 90°$, $\chi_{arr}^R = 0°$), UCAs ($N = 10$, $M = 8$, $\theta_{arr}^T = 90°$, $\phi_{arr}^T = 0°$, $\chi_{arr}^T = 0°$, $\theta_{arr}^R = 90°$, $\phi_{arr}^R = 0°$, $\chi_{arr}^R = 0°$), and URAs ($N_x = 5$, $N_y = 2$, $M_x = 3$, $M_y = 3$, $\theta_{arr}^T = 90°$, $\phi_{arr}^T = 0°$, $\chi_{arr}^T = 0°$, $\theta_{arr}^R = 90°$, $\phi_{arr}^R = 0°$, $\chi_{arr}^R = 0°$).

of the time-varying envelope vector

$$\tilde{\mathbf{z}}(t) = \text{vec}\left\{\left|\left[\tilde{\mathbf{H}}(t)\right]^\top\right|\right\} \quad (79)$$

$$= \begin{bmatrix} \tilde{z}_1(t) & \tilde{z}_2(t) & \dots & \tilde{z}_{MN}(t) \end{bmatrix}^\top. \quad (80)$$

By defining $\tilde{\mathbf{z}}(t)$ as in (79), the elements of the envelope vector are indexed such that the first N elements, $\{\tilde{z}_1(t), \tilde{z}_2(t), \dots \tilde{z}_N(t)\}$, describe the envelope of the channel response between the first receiving antenna and each of the N transmit antennas. The next N elements, $\{\tilde{z}_{N+1}(t), \tilde{z}_{N+2}(t), \dots \tilde{z}_{2N}(t)\}$, describe the same for the second receiving antenna and each of the N transmitting antennas, and so on. Thereby, and since the T_X is assumed to be free of local IOs, we can expect the elements of the

mth set $\{\tilde{z}_{(m-1)N+1}(t), \tilde{z}_{(m-1)N+2}(t), \dots \tilde{z}_{(m-1)N+N}(t)\}$, $m \in \{1, 2, \dots, M\}$, to be highly cross-correlated. This remark is supported by Fig. 3, where the high correlation between envelope waveforms associated with the same receiving antenna allows to identify $M = 9$ different segments in the vertical axis of each heatmap. These bands become less noticeable if the distance between elements of the transmitting antenna array is increased, or if the orientation of such an array changes, as in both cases the correlation between envelope waveforms will decay faster.

C. PERFORMANCE EVALUATION REGARDING THE SCCF

To gain further insight into the cross-correlation among the MIMO channel waveforms generated by the simulator, we present in Fig. 4 three surface plots of the reference model's

(a) DRSM & ULAs.

(b) RRSM & ULAs.

(c) DRSM & UCAs.

(d) RRSM & UCAs.

(e) DRSM & URAs.

(f) RRSM & URAs.
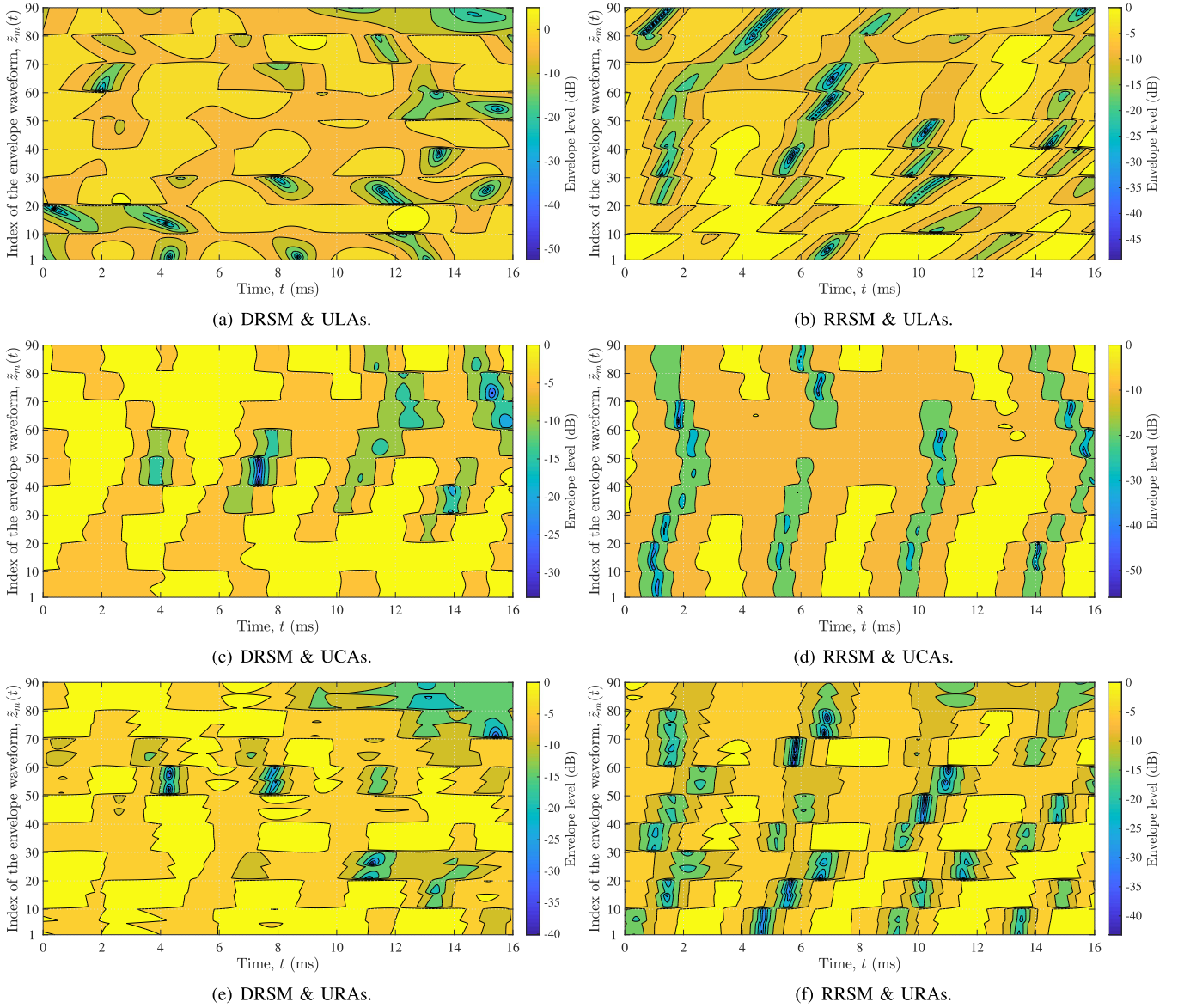
FIGURE 3. Heatmap of the envelope of a MIMO channel matrix realization produced by the SOC-based simulation model for the DRSM, the RRSM, the sphere scattering model, ULAs ($N = 10$, $M = 8$, $\theta_{arr}^T = 90°$, $\phi_{arr}^T = 90°$, $\chi_{arr}^T = 0°$, $\theta_{arr}^R = 90°$, $\phi_{arr}^R = 90°$, $\chi_{arr}^R = 0°$), UCAs ($N = 10$, $M = 8$, $\theta_{arr}^T = 90°$, $\phi_{arr}^T = 0°$, $\chi_{arr}^T = 0°$, $\theta_{arr}^R = 90°$, $\phi_{arr}^R = 0°$, $\chi_{arr}^R = 0°$), and URAs ($N_x = 5$, $N_y = 2$, $M_x = 3$, $M_y = 3$, $\theta_{arr}^T = 90°$, $\phi_{arr}^T = 0°$, $\chi_{arr}^T = 0°$, $\theta_{arr}^R = 90°$, $\phi_{arr}^R = 0°$, $\chi_{arr}^R = 0°$).
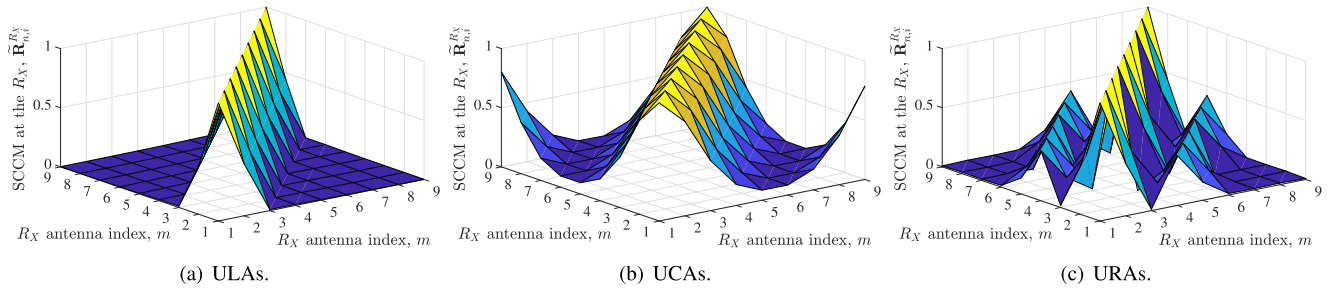
(a) ULAs.

(b) UCAs.

(c) URAs.

FIGURE 4. Surface plot of the reference model's SCCS, $\mathbf{R}_{n,i}^{R_X}$, for $n = i = N = 9$, the cylinder scattering model, and: (a) ULAs ($N = 10$, $M = 8$, $\theta_{arr}^T = 90°$, $\phi_{arr}^T = 90°$, $\chi_{arr}^T = 0°$, $\theta_{arr}^R = 90°$, $\phi_{arr}^R = 90°$, $\chi_{arr}^R = 0°$), (b) UCAs ($N = 10$, $M = 8$, $\theta_{arr}^T = 90°$, $\phi_{arr}^T = 0°$, $\chi_{arr}^T = 0°$, $\theta_{arr}^R = 90°$, $\phi_{arr}^R = 0°$, $\chi_{arr}^R = 0°$) and (b) URAs ($N_x = 5$, $N_y = 2$, $M_x = 3$, $M_y = 3$, $\theta_{arr}^T = 90°$, $\phi_{arr}^T = 0°$, $\chi_{arr}^T = 0°$, $\theta_{arr}^R = 90°$, $\phi_{arr}^R = 0°$, $\chi_{arr}^R = 0°$).
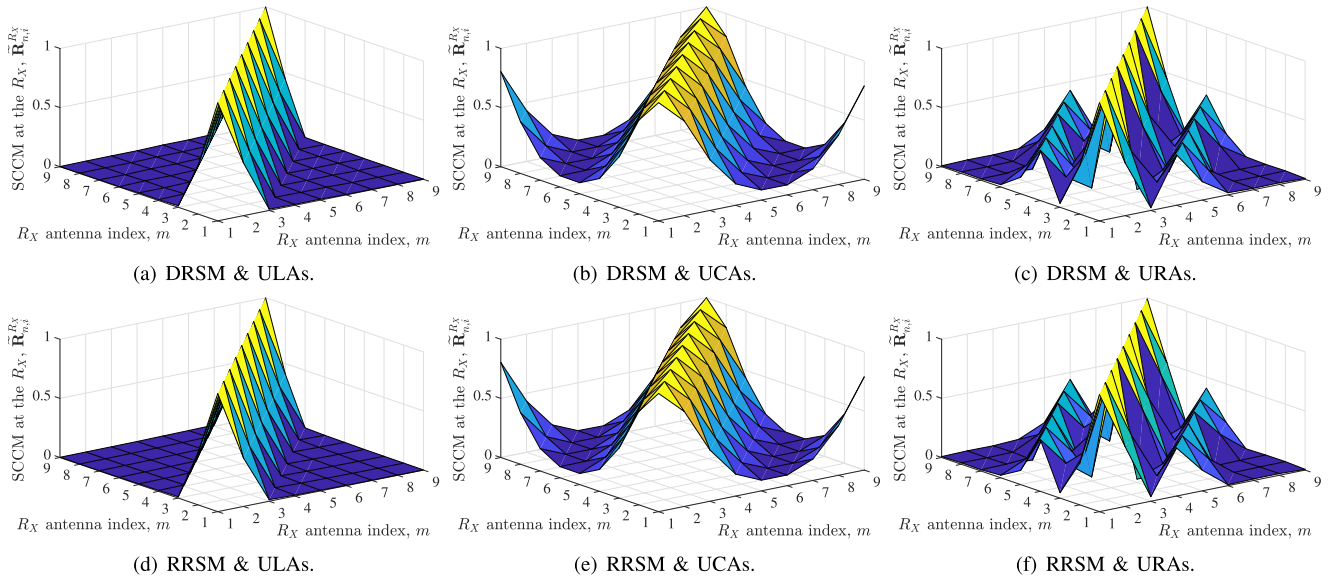
FIGURE 5. Surface plot of the simulation model's SCCS, $\widetilde{\mathbf{R}}_{n,i}^{R_X}$ for the DRSM, the RRSM, $n = i = N = 9$, the cylinder scattering model, and: (a) ULAs ($N = 10$, $M = 8$, $\theta_{\text{arr}}^T = 90°$, $\phi_{\text{arr}}^T = 90°$, $\chi_{\text{arr}}^T = 0°$, $\theta_{\text{arr}}^R = 90°$, $\phi_{\text{arr}}^R = 90°$, $\chi_{\text{arr}}^R = 0°$), (b) UCAs ($N = 10$, $M = 8$, $\theta_{\text{arr}}^T = 90°$, $\phi_{\text{arr}}^T = 0°$, $\chi_{\text{arr}}^T = 0°$, $\theta_{\text{arr}}^R = 90°$, $\phi_{\text{arr}}^R = 0°$, $\chi_{\text{arr}}^R = 0°$) and (b) URAs ($N_x = 5$, $N_y = 2$, $M_x = 3$, $M_y = 3$, $\theta_{\text{arr}}^T = 90°$, $\phi_{\text{arr}}^T = 0°$, $\chi_{\text{arr}}^T = 0°$, $\theta_{\text{arr}}^R = 90°$, $\phi_{\text{arr}}^R = 0°$, $\chi_{\text{arr}}^R = 0°$).

SCCS, $\mathbf{R}_{n,i}^{R_X}$, obtained by numerically evaluating (11) for $\Delta t = 0$ and the Nth transmitting antenna ($n = i = N = 9$), the cylinder scattering model, and the three array configurations.[5] The shape of the three correlation surfaces in Fig. 4 is in line with the geometry of the corresponding antenna array. For the ULA, the correlation between receiving antennas decays rapidly with the antenna separation, up to the point where the correlation is negligible when the antennas are located at the array's edges. For the UCA, the correlation shows a cyclic behavior, meaning that the correlation with the closest half of receiving antennas decays with the distance between antennas, but this behavior reverts for the farthest half, such that the correlation increases with the distance between antennas. For the URA, the shape of the SCCSs is a mixture between the ULA and URA. Similar trends are observed for the other SCCSs, $\mathbf{R}_{n,i}^{R_X}$, $n, i \in \{1, 2, \dots, N\}$, and for the SCCSs obtained for the sphere scattering model (these results are omitted for reasons of brevity).

Fig. 5 shows the surface plots of the simulation model's SCCSs, $\widetilde{\mathbf{R}}_{n,i}^{R_X} \in \mathbb{C}^{M \times M}$, for $n = i = N = 9$, the DRSM, the RRSM, and the same simulation cases presented in Fig. 4. By comparing the six surface plots shown in this figure with those presented in Fig. 4, we can observe that $\widetilde{\mathbf{R}}_{N,N}^{R_X} \approx \mathbf{R}_{N,N}^{R_X}$ for both the DRSM and the RRSM. While some differences can be noticed between the SCCS of the reference model and those produced by the DRSM, they are rather small. For the RRSM, the differences between $\widetilde{\mathbf{R}}_{N,N}^{R_X}$ and $\mathbf{R}_{N,N}^{R_X}$, which are due to the constrained DOA's range in the evaluation of (60), are even

less noticeable. These remarks are reinforced by the graphs shown in Fig. 6, where we present the element-wise squared absolute error (SAE), $\epsilon_{m,l}^{(N,l)}$, between the SCCSs $\widetilde{\mathbf{R}}_{N,N}^{R_X}$ and $\mathbf{R}_{N,N}^{R_X}$. Such an error is defined for any pair of SCCSs as

$$\epsilon_{m,l}^{(n,i)} = \left| \left\langle \mathbf{R}_{n,i}^{R_X} - \widetilde{\mathbf{R}}_{n,i}^{R_X} \right\rangle_{m,l} \right|^2 \tag{81}$$

for $m, l \in \{1, 2, \dots, M\}$ and $n, i \in \{1, 2, \dots, N\}$. The DRSM and the RRSM perform very well regarding $\epsilon_{m,l}^{(N,N)}$. However, the RRSM significantly outperforms the DRSM.

To assess the overall accuracy of these two methods in emulating the cross-correlation among the $M \cdot N = 90$ elements of the reference MIMO channel matrix, we present in Fig. 7 a box plot that summarizes the statistics of the SAE, $\epsilon_{m,l}^{(n,i)}$, between the $(M \cdot N)^2 = 8100$ elements of the SCCMs $\mathbf{R}$ and $\widetilde{\mathbf{R}}$ for the DRSM, the RRSM, and the six simulation cases. In addition, Table 2 presents the results of the corresponding Frobenius norm

$$\varepsilon_F = \left\| \mathbf{R} - \widetilde{\mathbf{R}} \right\|_F = \sum_{n=1}^{N} \sum_{i=1}^{N} \sum_{m=1}^{M} \sum_{l=1}^{M} \epsilon_{m,l}^{(n,i)} \tag{82}$$

of the error matrix between $\mathbf{R}$ and $\widetilde{\mathbf{R}}$. The results shown in Fig. 7 and Table 2 show that both PCM provide an excellent approximation to the reference model's SCCM, although we can observe again that the RRSM outperforms the DRSM for the three array configurations. These results also show that the performance of these PCM is influenced by the geometrical configuration of the propagation area. However, such an influence is rather moderate for the particular examples presented in this section. This was to be expected, as the channel's statistics are affected by the propagation environment's configuration through the functional dependence of

---

[5]It is important to stress that the SCCMs, $\mathbf{R}_{n,n}^{R_X}$, describe the correlation among the M receiving antennas for the nth transmitting antenna, whereas the heatmaps in Fig. 3 provide an idea of the correlation among the N transmitting antennas for each of the mth receiving antennas.
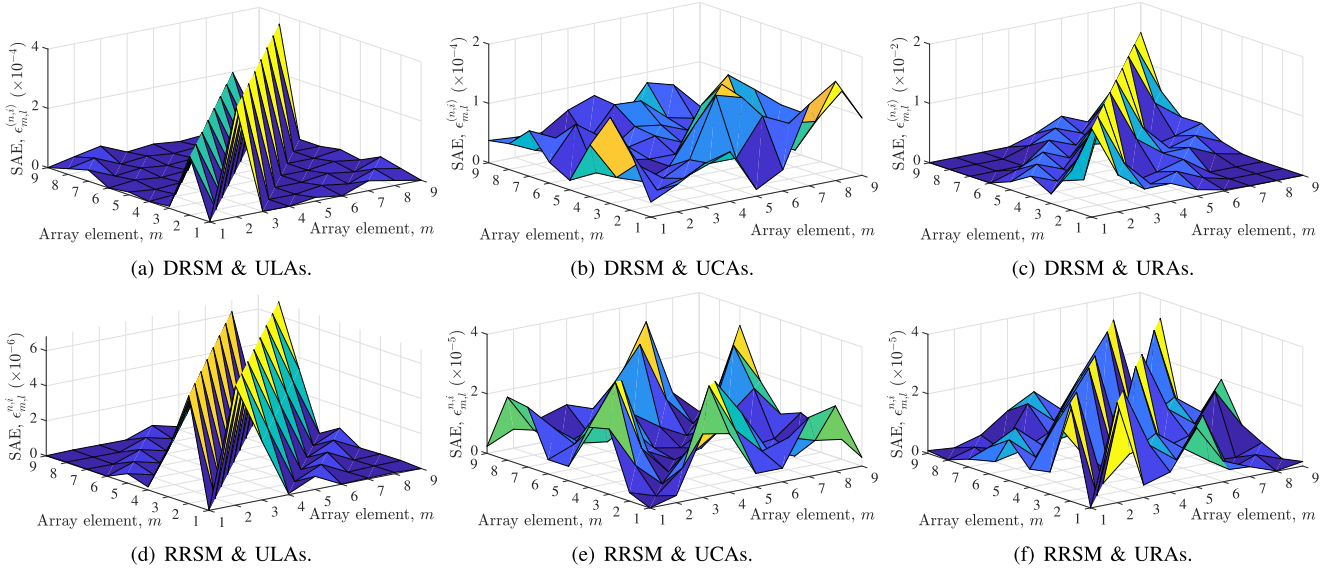
FIGURE 6. SAE of the SCCS for the DRSM, the RRSM, the cylinder scattering model, $n = 9$, and: (a) ULAs ($N = 10$, $M = 8$, $\theta_{arr}^T = 90°$, $\phi_{arr}^T = 90°$, $\chi_{arr}^T = 0°$, $\theta_{arr}^R = 90°$, $\phi_{arr}^R = 90°$, $\chi_{arr}^R = 0°$), (b) UCAs ($N = 10$, $M = 8$, $\theta_{arr}^T = 90°$, $\phi_{arr}^T = 0°$, $\chi_{arr}^T = 0°$, $\theta_{arr}^R = 90°$, $\phi_{arr}^R = 0°$, $\chi_{arr}^R = 0°$) and (c) URAs ($N_x = 5$, $N_y = 2$, $M_x = 3$, $M_y = 3$, $\theta_{arr}^T = 90°$, $\phi_{arr}^T = 0°$, $\chi_{arr}^T = 0°$, $\theta_{arr}^R = 90°$, $\phi_{arr}^R = 0°$, $\chi_{arr}^R = 0°$).
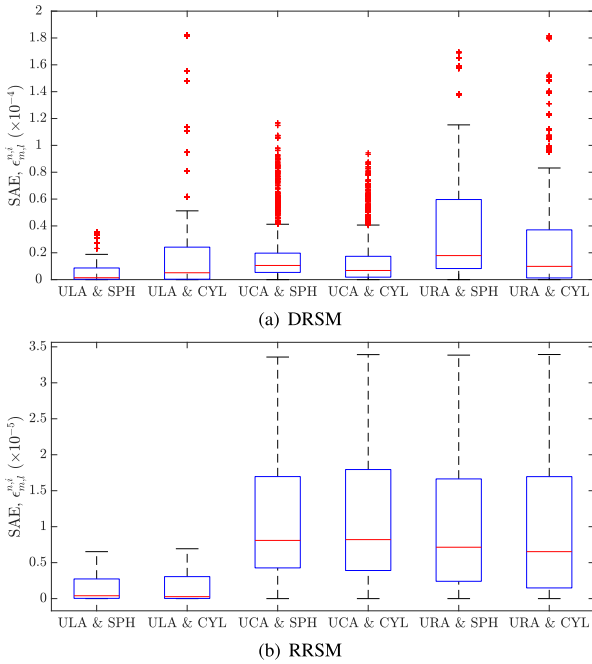
FIGURE 7. Box plot of the SAE between the SCCMs of the reference and simulation models for the (a) DRSM and (b) RRSM.

TABLE 2. Frobenius Norm of the Error Matrix $\mathbf{R} - \widetilde{\mathbf{R}}$ for the DRSM and RRSM

PCM	ULA		UCA		URA	
	SPH	CYL	SPH	CYL	SPH	CYL
DRSM	0.2107	0.4500	0.3590	0.3179	0.8121	0.6661
RRSM	0.1088	0.1160	0.2960	0.2960	0.2968	0.2959

simulators by taking into account the shape of the antenna arrays. Most of the papers presenting MIMO channel simulators assess the simulator's performance by considering a metric of error between the SCCMs of the reference and simulation models that depends only on the distance between the antennas (such as that in [21, Eq. (14)]). However, such a metric is adequate only if the T_X and R_X are equipped with ULAs. This metric is inadequate for other array configurations, because the error between $\mathbf{R}$ and $\widetilde{\mathbf{R}}$ is also influenced by the array's shape, as demonstrated by Fig. 7 and Table 2.

D. EMULATION OF THE TACF

Concerning the emulation of the channel's time-autocorrelation properties, we present in Fig. 8 a comparison between the TACF of the reference model, $R(\Delta t)$, and the TACF of the simulation model, $\widetilde{R}(\Delta t) = \widetilde{R}_{l,m,i,n}(\Delta t)\big|_{l=m,i=n}$, for the two PCMs. The curves shown in this figure were generated by evaluating (11), (25) and (60) for $\Delta t \in [0, 64]$ [ms], the sphere and the cylinder scattering model. The array's shape is not taken into account because according to the aforementioned three equations, it does not have any influence on the time-autocorrelation properties of $H_{m,n}(t)$ and $\widetilde{H}_{m,n}(t)$.

From Fig. 8, we can observe that the TACF of the reference model is essentially the same for the two geometrical

the IAOD, θ_T, and AAOD, ϕ_T, on the function $\mathcal{G}$ (see (16) and (17)). The effects of this function are essentially the same regardless of the particular form of $\mathcal{G}$ under the long-range assumption, $\mathcal{G}(\theta_R, \phi_R) \ll \|\mathbf{d}_{TR}\|$, $\forall \theta_R, \phi_R$, as one may infer from (18) and (19). Nevertheless, we point out that the effects of the propagation area's geometrical configuration will be exacerbated for short-range links.

The results shown in Fig. 7 and Table 2 also demonstrate the importance of evaluating the performance of MIMO channel

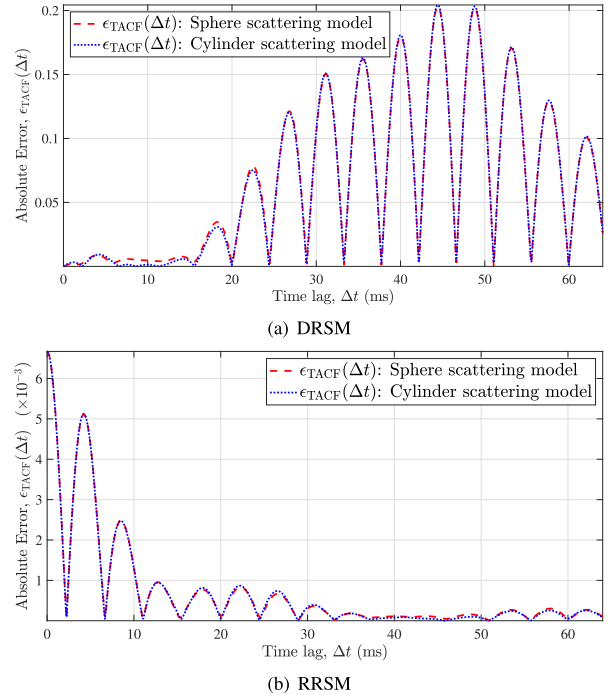(a) DRSM

(a) DRSM

(b) RRSM

(b) RRSM

FIGURE 8. Comparison between the TACF of the reference and simulation models for (a) the DRSM and (b) the RRSM with an ULA, and $\theta_{arr}^T = 90°$, $\phi_{arr}^T = 90°$ and $\chi_{arr}^T = 0°$.

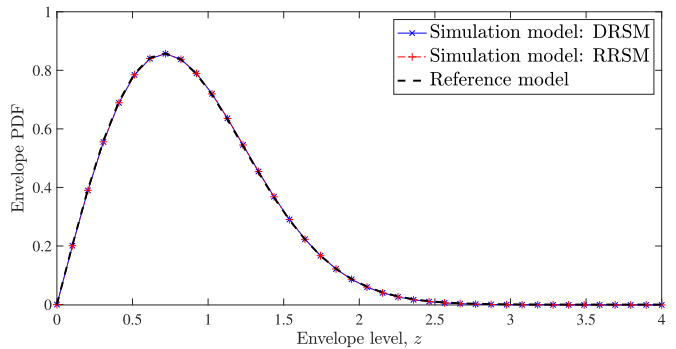**FIGURE 9.** Absolute error between the TACF of the reference and simulation models for the (a) the DRSM and (b) the RRSM with an ULA oriented toward $\theta_{arr}^T = 90°$, $\phi_{arr}^T = 90°$ and $\chi_{arr}^T = 0°$.

scattering models. This is in line with the remarks we made in the previous subsection about the influence of the propagation area's geometrical configuration on the SCCM. However, Fig. 8 shows that the channel's TACF is even less sensitive than the SCCM to a change in the geometrical configuration of the propagation environment; this is true at least if the long-range assumption is valid. Aside from this, a comparison between the curves of $R(\Delta t)$ and $\widetilde{R}(\Delta t)$ show that both PCM provide an excellent approximation to the reference model's TACF. While the curves of $\widetilde{R}(\Delta t)$ obtained by applying the DRSM diverge from those of $R(\Delta t)$ for $\Delta t > 17$ [ms], the fitting between both TACF is very good for smaller values of Δt. The quality of the approximation is much better for the RRSM, such that the differences between $\widetilde{R}(\Delta t)$ and $R(\Delta t)$ are imperceptible from Fig. 8(b), which indicates that the value of $\eta = 1$ is a proper choice for evaluating (60) with a truncated DOA's range. Fig. 9 shows the absolute error

$$\epsilon_{TACF}(\Delta t) = \left| \widetilde{R}(\Delta t) - R(\Delta t) \right| \qquad (83)$$

between the TACF's of the reference and simulation models for the DRSM and the RRSM. The error $\epsilon_{TACF}(\Delta t)$ obtained by applying the DRSM is small for small values of Δt, although it increases significantly for large values of Δt. While the error obtained for the RRSM is not exactly equal to zero, it is very small across the whole observation interval $\Delta t \in [0, 64]$ [ms].

FIGURE 10. Absolute error between the envelope PDFs of the reference and simulation models for (a) the DRSM and (b) the RRSM.

E. PERFORMANCE EVALUATION REGARDING THE ENVELOPE PDF

Finally, Fig. 10 presents a comparison between the envelope PDF of the reference model, $f_Z(z)$, and that of the simulation model, $f_{\widetilde{Z}}(z)$, by applying the DRSM and the RRSM. For the former PCM, the curve of $f_{\widetilde{Z}}(z)$ was generated by numerically evaluating (23), with the improper integral truncated at a maximum value of $x = 10$. For the latter PCM, we evaluated the PDF in (48) by making the upper limit of the innermost improper integral equal to $\sup\{f_{DOA}^R(\theta, \phi)\}$ whereas that of the outermost integral was set equal to 10. The propagation environment and the antenna arrays are irrelevant for the analysis of the envelope PDF, as these factors have not effect on this statistical function, as in the case of the TACF.

From the curves shown in Fig. 10, we can conclude that $f_Z(z) = f_{\tilde{Z}}(z)$ for the DRSM and the RRSM, as there are not visible differences between the curves of $f_Z(z)$ and those of $f_{\tilde{Z}}(z)$ produced by any of these two PCMs. However, this observation applies only to the particular setup of our simulation examples; the quality of the approximation $f_Z(z) \approx f_{\tilde{Z}}(z)$ should be evaluated on a case-by-case basis, as this relationship could worsen if a different joint-PDF is employed to model the DOA, or if the DOA's range is partitioned by considering a different number of segments K_θ and K_ϕ (which determines the number of cisoids, K).

VI. CONCLUDING REMARKS

In this paper, we presented two new PCMs for the design of SOC-based simulators for 3D MIMO M2M fading channels. One method, called the DRSM, is specific for the ergodic simulation of WSS channels, whereas the other method, called the RRSM, can be applied to the simulation of both WSS channels and non-WSS channels having an underlying blockwise-stationary structure. These two methods are formulated to admit any given geometrical configuration of the propagation area and the antenna arrays. To demonstrate the excellent performance of both PCMs, we presented several simulation examples regarding the emulation of the SCCM, the TACF and the envelope PDF of the reference MIMO channel model. Such examples involved six different simulation cases comprising two well-known geometrical scattering models, namely the sphere and cylinder models, and three antenna array configurations: the ULA, the UCA and the URA. Our results suggest that the DRSM and RRSM perform the same w.r.t. the emulation of the channel's envelope PDF, although the latter method performs better than the former concerning the emulation of the SCCM and TACF. In fact, the SAE obtained by applying the RRSM is two-order of magnitudes smaller than that obtained with the DRSM for the case of non-ULAs.

While not shown in this paper, we note that the DRSM and RRSM have a linear time complexity because Algorithms 1 and 2 involve operations having a linear time complexity. Likewise, the validity of the mathematical formulas that characterize the ST-CCF and envelope PDF of both the reference model and the SOC-based simulation model has been verified empirically, although the results were not included in this paper to simplify our discussions. Further work is necessary, nonetheless, to assess the convergence rate between: (i) the time averages and the ensemble averages of the ergodic SOC-simulation model when applying the DRSM, (ii) the variance of the error between the ensemble ST-CCF and the average of the ST-CCF of the sample functions generated by the RRSM. In addition, the extension of the DRSM and the RRSM w.r.t. the simulation of frequency-selective channels needs to be addressed, as the simulation of such channels is important for the performance analysis of modern wideband transmission systems. We leave these problems open for future research.

APPENDIX A
VECTOR REPRESENTATION OF THE ANTENNA ARRAY GEOMETRY

Our reference channel model and the proposed channel simulation methods are formulated to admit a wide variety of antenna array configurations. For the purposes of demonstration, we consider in this paper the ULA, UCA and URA configurations [40]. This appendix presents a short description of these three arrays.

A1 BASIC CONFIGURATIONS

For the ULA configuration, we assume that the array is comprised of M antenna elements arranged linearly along the $\hat{\mathbf{z}}$ axis, with an inter-element distance equal to $\Delta_A = L_a/(M-1)$, where L_a is the total length of the array, as shown in Fig. 11. For this basic configuration, the position of the mth antenna element, as seen from the array's center of mass,[6] $\mathcal{O}_A$, can be modeled in rectangular coordinates as:

$$\mathbf{a}_m^0 = \hat{\mathbf{z}} A_m \tag{84}$$

where

$$A_m = \frac{\Delta_A}{2}(2m - M - 1) \tag{85}$$

for $m \in \{1, 2, \ldots, M\}$.

Most of the existing SOC-based MIMO channel simulator have been designed upon the ULA configuration. However, another important configuration, which has received comparatively less attention is the UCA. We characterize this latter antenna array by assuming a total of M antenna elements located on the x-y plane and arranged circularly around the z-axis, as shown in Fig. 12. Thereby, the position of the mth antenna element w.r.t. $\mathcal{O}_A$ can be written as:

$$\mathbf{a}_m^0 = A\left[\hat{\mathbf{x}}\cos\left(\frac{2\pi(m-1)}{M}\right) + \hat{\mathbf{y}}\sin\left(\frac{2\pi(m-1)}{M}\right)\right] \tag{86}$$

for $M \geq 2$ and $m \in \{1, 2, \ldots, M\}$, where A indicates the distance between $\mathcal{O}_A$ and any array element. We notice that the UCA collapses to a 2-element ULA, a 3-element triangular array, and a 4-element URA if $m = 2$, $m = 3$, and $m = 4$, respectively. For a given distance, $\Delta_A > 0$, between adjacent antenna elements, the radius of the UCA can be determined as follows

$$A = \frac{\Delta_A}{2\sin\left(\frac{2\pi(m-1)}{M}\right)}. \tag{87}$$

---

[6]Antenna arrays are described in this appendix without distinction of whether the array is in transmitting or receiving mode.
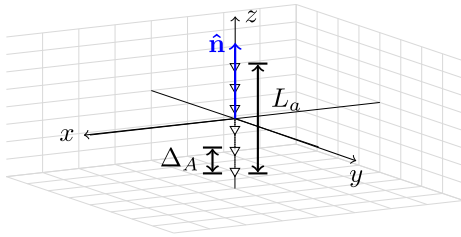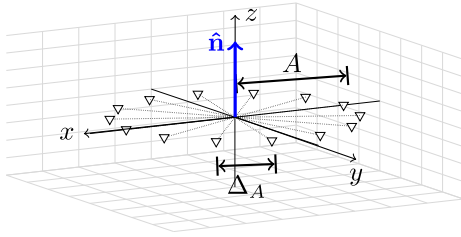
FIGURE 11. Basic geometry of an ULA array with $M = 6$.
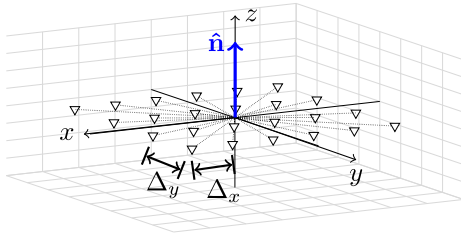

FIGURE 12. Basic geometry of an UCA array with $M = 14$.

FIGURE 13. Basic geometry of an URA array with $M_x = 6$ and $M_y = 4$.

FIGURE 14. Geometry of an ULA with $M = 6$ elements and oriented toward a direction ($\theta_{\mathrm{arr}} = 0°$, $\phi_{\mathrm{arr}} = 0°$) ($\chi = 0$).

(a) UCA with $M = 14$.

(b) URA with $M_x = 6$ and $M_y = 4$.

FIGURE 15. Geometries of (a) UCA and (b) URA oriented toward a direction ($\theta_{\mathrm{arr}} = 45°$, $\phi_{\mathrm{arr}} = 55°$) with $\chi_{\mathrm{arr}} = 0$ (unrotated array).

The URA is another configuration that has gained relevance in recent years as a convenient radiating structure for fifth-generation communication systems. For this array, we consider a basic configuration involving $M_y \in \{2, 3, \ldots\}$ ULAs which are located parallel to the y-axis and equally spaced apart from one another, as shown in Fig. 13. Each ULA is further comprised of $M_x \in \{2, 3, \ldots\}$ uniformly-spaced antenna elements. Under these considerations, the position of the mth antenna element can be written as

$$\mathbf{a}_m^0 = \hat{\mathbf{x}} \frac{\Delta_x}{2} \left[2 \left(m - M_x \left\lfloor \frac{m-1}{M_x} \right\rfloor \right) - M_x - 1 \right]$$
$$+ \hat{\mathbf{y}} \frac{\Delta_y}{2} \left[2 \left\lceil \frac{m}{M_x} \right\rceil - M_y - 1 \right] \quad (88)$$

for $m \in \{1, 2, \ldots, M_x \cdot M_y\}$, where

$$\Delta_x = \frac{L_x}{M_x - 1}, \qquad \Delta_y = \frac{L_y}{M_y - 1}. \quad (89)$$

The variables L_x and L_y stand for the length of the URA in the dimensions of the x and y variables.

A2 ARBITRARILY ORIENTED CONFIGURATIONS

The basic array configurations of the previous subsection are specified for a particular array orientation. However, the array can easily be oriented toward any given direction of interest if the vectors $\mathbf{a}_m^0$ defined in (84), (86) and (88) are transformed
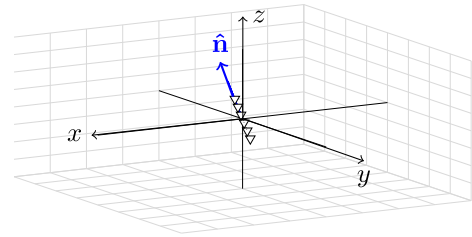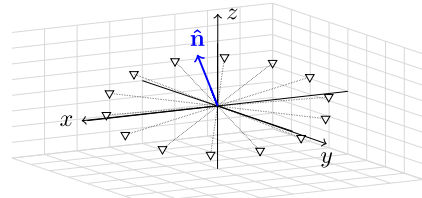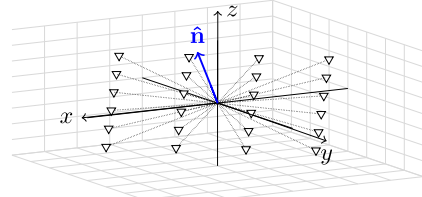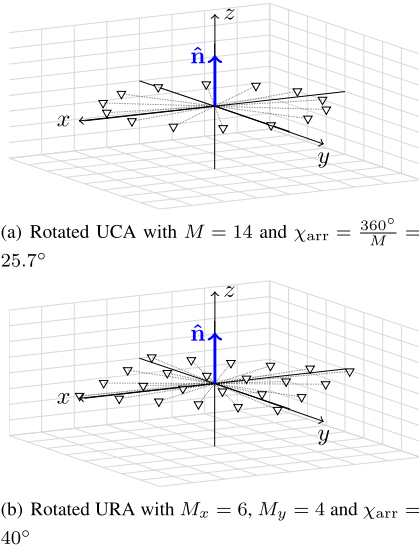
according to

$$\mathbf{a}_m = \mathbf{M}_z(\phi_{\mathrm{arr}}) \mathbf{M}_y(\theta_{\mathrm{arr}}) \mathbf{M}_z(\chi_{\mathrm{arr}}) \mathbf{a}_m^0 \quad (90)$$

where $\theta_{\mathrm{arr}} \in [0, \pi)$ and $\phi_{\mathrm{arr}} \in [0, 2\pi)$ describe the inclination and azimuth, respectively, of the direction toward which the array is oriented, whereas the angle $\chi_{\mathrm{arr}} \in [0, 2\pi)$ stands for the rotation of the array about its axis (vector $\hat{\mathbf{n}}$). Note that this latter angle does not produce any effects on the ULA. The matrices $\mathbf{M}_z(\chi)$ and $\mathbf{M}_y(\chi)$ characterize standard counterclockwise rotations by an angle χ about the z and y axes, respectively [41]. These matrices are given as:

$$\mathbf{M}_y(\chi) = \begin{bmatrix} \cos\chi & 0 & \sin\chi \\ 0 & 1 & 0 \\ -\sin\chi & 0 & \cos\chi \end{bmatrix} \quad (91)$$

$$\mathbf{M}_z(\chi) = \begin{bmatrix} \cos\chi & -\sin\chi & 0 \\ \sin\chi & \cos\chi & 0 \\ 0 & 0 & 1 \end{bmatrix}. \quad (92)$$

Figs. 14 and 15 show examples of the three arrays configurations by considering $\theta_{\mathrm{arr}} = 45°$, $\phi_{\mathrm{arr}} = 55°$, and $\chi_{\mathrm{arr}} = 0°$. In turn, Fig. 16 show the UCA and URA oriented toward the direction $\theta_{\mathrm{arr}} = 45°$, $\phi_{\mathrm{arr}} = 55°$, and rotated by an angle χ_{arr}.

(a) Rotated UCA with $M = 14$ and $\chi_{\text{arr}} = \frac{360°}{M} = 25.7°$

(b) Rotated URA with $M_x = 6$, $M_y = 4$ and $\chi_{\text{arr}} = 40°$

FIGURE 16. Geometries of (a) UCA and (b) URA oriented toward the default direction ($\theta_{\text{arr}} = 0°$, $\phi_{\text{arr}} = 0°$) and rotated about the array's axis by an angle χ_{arr}.

APPENDIX B
GEOMETRICAL CONFIGURATIONS OF THE PROPAGATION AREA
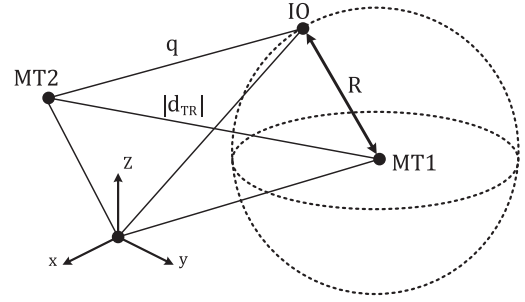
B1 THE GEOMETRICAL SPHERE SCATTERING MODEL

The sphere scattering model is built on the assumptions that only one mobile terminal (MT) (either the T_X or the R_X) is surrounded by local IOs, and that such IOs are initially located at the same distance R from this MT [31], as shown in Fig. 17 (MT1 stands for the MT surrounded by local IOs, whereas MT2 is the terminal that is free of local IOs). For this scattering model, the function that characterizes the distance, q, from the IOs to the MT that is free from local scatters is given by:

$$\mathcal{G}(\theta_R, \phi_R) = R, \quad \forall \theta_R \in [0, \pi), \phi_R \in [0, 2\pi). \tag{93}$$

B2 THE GEOMETRICAL CYLINDER SCATTERING MODEL

The cylinder model [42, Sec. 5.12.1] is also built on the assumption that one MT is surrounded by local IOs whereas the other is free from IOs. In addition, the IOs are assumed to be located on an imaginary cylindrical surface of radius $R > 0$ and height $h_{\text{cyl}} > 0$. The MT within such a cylinder is further assumed to be initially located at a height $0 < h_{\text{MT}} < h_{\text{cyl}}$ and on the cylinder's axis, as shown in Fig. 18. For this geometrical model, the distance, q, between the IOs to the MT that is free from local scatters is characterized by the function:

$$\mathcal{G}(\theta_R, \phi_R) = \begin{cases} \frac{h_{\text{cyl}} - h_{\text{MT}}}{\cos \theta_R}, & \forall \phi_R \in [0, 2\pi), 0 < \theta_R < \theta_{\text{top}} \\ \frac{R}{\sin \theta_R}, & \forall \phi_R \in [0, 2\pi), \theta_{\text{top}} < \theta_R < \theta_{\text{bot}} \\ -\frac{h_{\text{MT}}}{\cos \theta_R}, & \forall \phi_R \in [0, 2\pi), \theta_{\text{bot}} < \theta_R < \pi \end{cases}$$
$$\tag{94}$$

FIGURE 17. Illustration of the geometrical sphere scattering model.
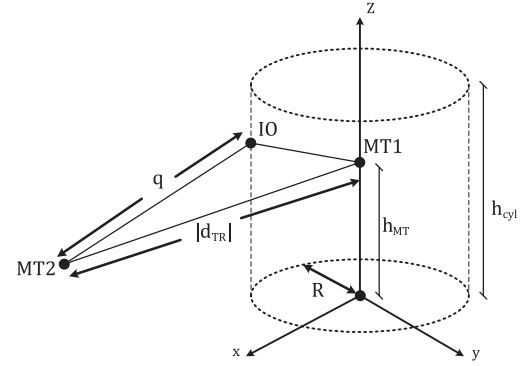
FIGURE 18. Illustration of the geometrical cylinder scattering model.

where:

$$\theta_{\text{top}} = \pi - \arctan\left(\frac{R}{h_{\text{MT}}}\right) \tag{95}$$

$$\theta_{\text{bot}} = \arctan\left(\frac{R}{h_{\text{cyl}} - h_{\text{MT}}}\right). \tag{96}$$

REFERENCES

[1] S. O. Rice, "Mathematical analysis of random noise," *Bell Syst. Tech. J.*, vol. 23, pp. 282–332, 1944.

[2] S. O. Rice, "Mathematical analysis of random noise," *Bell Syst. Tech. J.*, vol. 24, pp. 46–156, 1945.

[3] M. Pätzold and B. Talha, "On the statistical properties of sum-of-cisoids-based mobile radio channel simulators," in *Proc. 10th Int. Symp. Wireless Pers. Multimedia Commun.*, 2007, pp. 394–400.

[4] S. Fard, "Single-field programmable gate array simulator for geometric multiple-input multiple-output fading channel models," *IET Commun.*, vol. 5, no. 9, pp. 1246–1254, Jun. 2011.

[5] L. Vela-Garcia, J. Vázquez Castillo, R. Parra-Michel, and M. Pätzold, "An accurate hardware sum-of-cisoids fading channel simulator for isotropic and non-isotropic mobile radio environments," *Modelling Simul. Eng.*, vol. 2012, 2012, Art. no. 542198.

[6] Á. E. Ruiz-García, C. A. Gutierrez, J. Cortez, E. Ruiz-Ibarra, and J. Vázquez-Castillo, "SDR-based wideband emulator of non-WSSUS channels for vehicular communications," *Circuits, Syst., Signal Process.*, vol. 41, no. 7, pp. 3832–3852, 2022.

[7] M. Pätzold, *Mobile Radio Channels*, 2nd ed. Chichester, U.K.: Wiley, 2011.

[8] P. K. Singh, S. K. Nandi, and S. Nandi, "A tutorial survey on vehicular communication state of the art, and future research directions," *Veh. Commun.*, vol. 18, 2019, Art. no. 100164.

[9] Q. Zhu et al., "A novel 3D non-stationary wireless MIMO channel simulator and hardware emulator," *IEEE Trans. Commun.*, vol. 66, no. 9, pp. 3865–3878, Sep. 2018.

[10] K. Jiang, X. Chen, Q. Zhu, L. Chen, D. Xu, and B. Chen, "A novel simulation model for nonstationary rice fading channels," *Wireless Commun. Mobile Comput.*, vol. 2018, pp. 1–9, 2018.

[11] J. J. Jaime-Rodríguez, C. A. Gómez-Vega, C. A. Gutiérrez, J. M. Luna-Rivera, D. U. Campos-Delgado, and R. Velázquez, "A non-WSSUS channel simulator for V2X communication systems," *Electronics*, vol. 9, no. 8, 2020, Art. no. 1190.

[12] C. A. Gutiérrez, J. T. Gutiérrez-Mena, J. M. Luna-Rivera, D. U. Campos-Delgado, R. Velázquez, and M. Pätzold, "Geometry-based statistical modeling of non-WSSUS mobile-to-mobile Rayleigh fading channels," *IEEE Trans. Veh. Technol.*, vol. 67, no. 1, pp. 362–377, Jan. 2018.

[13] J. T. Gutiérrez-Mena, C. A. Gutiérrez, J. M. Luna-Rivera, D. U. Campos-Delgado, and J. Vázquez-Castillo, "A novel geometrical model for non-stationary MIMO vehicle-to-vehicle channels," *IETE Tech. Rev.*, vol. 36, no. 1, pp. 27–38, 2019.

[14] M. Centenaro, L. Vangelista, A. Zanella, and M. Zorzi, "Long-range communications in unlicensed bands: The rising stars in the IoT and smart city scenarios," *IEEE Wireless Commun.*, vol. 23, no. 5, pp. 60–67, Oct. 2016.

[15] H. Jiang, D. Qu, J. Ding, Z. Wang, H. He, and H. Chen, "Enabling LP-WAN massive access: Grant-free random access with massive MIMO," *IEEE Wireless Commun.*, vol. 29, no. 4, pp. 72–77, Aug. 2022.

[16] J. J. Lopez-Salamanca, L. O. Seman, M. D. Berejuck, and E. A. Bezerra, "Finite-state Markov chains channel model for CubeSats communication uplink," *IEEE Trans. Aerosp. Electron. Syst.*, vol. 56, no. 1, pp. 142–154, Feb. 2020.

[17] B. O. Hogstad, C. A. Gutiérrez, M. Pätzold, and P. M. Crespo, "Classes of sum-of-cisoids processes and their statistics for the modelling and simulation of mobile fading channels," *EURASIP J. Wireless Commun. Netw.*, vol. 2013, no. 2013, pp. 1–15, May 2013.

[18] C. A. Gutiérrez, M. Pätzold, A. Sandoval, and C. Delgado-Mata, "An ergodic sum-of-cisoids simulator for multiple uncorrelated Rayleigh fading channels under generalized scattering conditions," *IEEE Trans. Veh. Technol.*, vol. 61, no. 5, pp. 2375–2382, Jun. 2012.

[19] W. Wang, H. Wang, Y. Wu, and Y. Liu, "Novel deterministic angular sampling methods for 3D channel models," *IEEE Commun. Lett.*, vol. 25, no. 6, pp. 1756–1760, Jun. 2021.

[20] C. A. Gutiérrez and M. Pätzold, "The design of sum-of-cisoids rayleigh fading channel simulators assuming non-isotropic scattering conditions," *IEEE Trans. Wireless Commun.*, vol. 9, no. 4, pp. 1308–1314, Apr. 2010.

[21] C. A. Gutiérrez and M. Cabrera-Bean, "Deterministic simulation of flat-fading MIMO wireless channels under non-isotropic scattering conditions," in *Proc. IEEE 17th Int. Symp. Pers., Indoor, Mobile Radio Commun.*, 2007, pp. 1–5.

[22] C. A. Gutiérrez and M. Pätzold, "The generalized method of equal areas for the design of sum-of-cisoids simulators for mobile Rayleigh fading channels with arbitrary doppler spectra," *Wireless Commun. Mobile Comput.*, vol. 13, no. 10, pp. 951–966, Jun. 2011, doi: 10.1002/wcm.1154.

[23] M. Pätzold and B. O. Hogstad, "A space-time channel simulator for MIMO channels based on the geometrical one-ring scattering model," *Wireless Commun. Mob. Comput.*, vol. 4, no. 7, pp. 727–737, Nov. 2004.

[24] C. A. Gutierrez, O. Caicedo, and D. U. Campos-Delgado, "5G and beyond: Past, present and future of the mobile communications," *IEEE Latin Amer. Trans.*, vol. 19, no. 10, pp. 1702–1736, Oct. 2021.

[25] R. A. Fabián-Rodríguez and C. A. Gutiérrez, "The Riemann sum method for the SOC-based simulation of 3D MIMO fading channels," in *Proc. 4th South Amer. Conf. Visible Light Commun.*, 2023, pp. 1–6.

[26] E. Basar, M. Di Renzo, J. De Rosny, M. Debbah, M.-S. Alouini, and R. Zhang, "Wireless communications through reconfigurable intelligent surfaces," *IEEE Access*, vol. 7, pp. 116753–116773, 2019.

[27] F. R. Castillo-Soria et al., "Precoding for RIS-assisted multi-user MIMO-DQSM transmission systems," *Future Internet*, vol. 15, no. 9, 2023, Art. no. 299.

[28] A. Bansal, N. Agrawal, K. Singh, C.-P. Li, and S. Mumtaz, "RIS selection scheme for UAV-based multi-RIS-aided multiuser downlink network with imperfect and outdated CSI," *IEEE Trans. Commun.*, vol. 71, no. 8, pp. 4650–4664, Aug. 2023.

[29] A. Papoulis and S. U. Pillai, *Probability, Random Variables and Stochastic Processes*, 4th ed. New York, NY, USA: McGraw-Hill, 2002.

[30] K. V. Mardia and P. E. Jupp, *Directional Statistics*. Chichester, U.K.: Wiley, 1999.

[31] E. Assiimwe and Y. W. Marye, "A mobility model for a 3D non-stationary geometry cluster-based channel model for high speed trains in MIMO wireless channels," *Sensors*, vol. 22, no. 24, 2022, Art. no. 10019.

[32] A. G. Zajić and G. L. Stüber, "Three-dimensional modeling and simulation of wideband MIMO mobile-to-mobile channels," *IEEE Trans. Wireless Commun.*, vol. 8, no. 3, pp. 1260–1275, Mar. 2009.

[33] A. Abdi and M. Kaveh, "A space-time correlation model for multielement antenna systems in mobile fading channels," *IEEE Trans. Veh. Technol.*, vol. 20, no. 3, pp. 550–560, Apr. 2002.

[34] C. A. Gutiérrez, H. Rodríguez, and M. Miranda-Burgos, "Analysis of error in the estimation of the temporal ACF of ergodic sum-of-cisoids simulators for mobile fading channels," in *Proc. IEEE Int. Conf. Signal Process. Commun. Syst.*, 2011, pp. 1–9.

[35] C. F. Mecklenbrauker et al., "Vehicular channel characterization and its implications for wireless system design and performance," *Proc. IEEE*, vol. 99, no. 7, pp. 1189–1212, Jul. 2011.

[36] R. E. Haddad, R. Fakhreddine, and C. Lécot, *Chapter 12, Stratified Monte Carlo Integration*. Berlin, Germany: De Gruyter, 2013, pp. 105–114, doi: 10.1515/9783110293586.105.

[37] Y. R. Zheng and C. Xiao, "Simulation models with correct statistical properties for Rayleigh fading channels," *IEEE Trans. Commun.*, vol. 51, no. 6, pp. 920–928, Jun. 2003.

[38] R. von Mises, "Über die 'Ganzzahligkeit' der Atomgewichte und verwandte Fragen," *Physikalische Zeitschrift*, vol. 19, pp. 490–500, 1918.

[39] R. Janaswamy, *Radiowave Propagation and Smart Antennas for Wireless Communications*. Boston, MA, USA: Kluwer Academic Publishers, 2001.

[40] R. L. Haupt, *Antenna Arrays: A Computational Approach*. Hoboken, NJ, USA: Wiley, 2010.

[41] S. L. Altmann, *Rotations, Quaternions, and Double Groups*. New York, NY, USA: Dover Pub., 2005.

[42] J. D. Parsons, *The Mobile Radio Propagation Channel*, 2nd ed. Chichester, U.K.: Wiley, 2000.

CARLOS A. GUTIÉRREZ (Senior Member, IEEE) received the B.E. degree in electronics and digital communication systems from the Universidad Autoónoma de Aguascalientes, Aguascalientes, Mexico, in 2002, the Advanced Studies Diploma in signal processing and communication theory from the Universidad Politécnica de Cataluña, Barcelona, Spain, in 2005, the M.S. degree in electronics and telecommunications from CICESE, Ensenada, Mexico, in 2006, and the Ph.D. degree in mobile communication systems from the University of Agder, Kristiansand, Norway, in 2009. From 2009 to 2011, he was with the School of Engineering, Universidad Panamericana, Aguascalientes. Since 2012, he has been with the Faculty of Science, Universidad Autónoma de San Luis Potosí, San Luis Potosí, México. His research interests include modeling, simulation, and measurement of wireless channels, antenna design, electromagnetic wave propagation, vehicular communications, and radio sensing for vehicular applications and human activity recognition. Dr. Gutiérrez has held different positions in organizing and technical program committees of various international conferences. He was an Expert Evaluator for the European Commission and CONACYT (Mexico), an Associate Editor for the *IEEE Vehicular Technology Magazine*, and the Guest Editor of several international journals. He was the recipient of three best paper awards. He is a Member of the Technical Committee on Propagation of the IEEE Vehicular Technology Society.

RAÚL A. FABÍAN-RODRÍGUEZ received the B.S. degree in telecommunications engineering from the Universidad Autónoma de San Luis Potosí, San Luis Potosí, Mexico, in 2023. He is currently working toward the M.S. degree in electronic engineering (major in telecommunications) with the Universidad Autónoma de San Luis Potosí. His research interests include vehicle-to-vehicle communications, anisotropic and isotropic 3D channel simulators, electromagnetic wave propagation, and wireless communications.

FRANCISCO R. CASTILLO-SORIA received the B.E. degree in electronics and communication and the M.S. degree in telecommunications engineering from the National Polytechnic Institute, ESIME, Mexico City, Mexico, in 2000 and 2004 respectively, and the Ph.D. degree in electronics and telecommunications from the CICESE Research Center, Ensenada, Mexico, in 2015. From 2005 to 2016, he was with the Department of Computer Engineering, Universidad del Istmo, Campus Tehuantepec, Oaxaca, Mexico. His research interests include spatial/index modulation, media-based modulation, RIS/relay-assisted systems, MIMO-OFDM systems, and signal processing for mobile communications. Since 2017, he has been a full-time Professor with the Faculty of Science, Universidad Autónoma de San Luis Potosí, San Luis Potosí, México. He is a Member of the Mexican National System of Researchers, level I. He was the invited Editor of several JCR journals.

PABLO ADASME was born in Santiago, Chile, in 1972. He received the title of Industrial Engineer together with B. Sc. and M. Sc. degrees from Universidad de Santiago de Chile, Santiago, Chile, in 2000 and 2003, respectively, and the Ph.D. degree in computer science from the Universitè de Paris Sud 11, Paris, France, in 2010. He is currently an Associate Researcher and Full Professor of computer science with the Electrical Engineering Department of the Universidad de Santiago de Chile. His research interests include deterministic and stochastic combinatorial optimization problems applied to a diverse range of engineering domains including wireless communications, signal processing, network design, and energy problems.

CESAR A. AZURDIA-MEZA (Member, IEEE) received the B.Sc. degree in electronics engineering from Universidad del Valle de Guatemala, Guatemala City, Guatemala, in 2005, and the M.Sc. degree in electrical engineering from Linnaeus University, Växjö, Sweden, in 2009, and the Ph.D. degree in electronics and radio engineering, Kyung Hee University, Seoul, South Korea, in 2013. He joined the Department of Electrical Engineering, University of Chile, Santiago, Chile, as an Assistant Professor in 2013, and an Associate Professor in 2021, where he is currently lecturing on wireless and mobile communication systems. His research interests include Nyquist's ISI criterion, OFDM-based systems, SC-FDMA, visible light communication systems, vehicular communications, 5G and beyond enabling technologies, and signal processing techniques for communication systems. Dr. Azurdia has been the Principal Investigator of several national and international research grants. He was a Technical Program Committee Member of multiple conferences and Reviewer of journals such as IEEE COMMUNICATIONS LETTERS, IEEE TRANSACTIONS ON WIRELESS COMMUNICATIONS, *Wireless Personal Communications*, IEEE ACCESS, *IET Communications*, and *EURASIP Journal on Advances in Signal Processing*. He is an IEEE Communications Society Member and Member of the IEICE Communications Society. He was the co-recipient of the 2019 IEEE LATINCOM Best Paper Award and 2016 IEEE CONESCAPAN Best Paper Award.